

INTEGRATION OF A GaAs/AlGaAs SQW LASER AND
A TAPERED WAVEGUIDE COUPLER

By

SUNING XIE

A DISSERTATION PRESENTED TO THE GRADUATE SCHOOL
OF THE UNIVERSITY OF FLORIDA IN PARTIAL FULFILLMENT
OF THE REQUIREMENTS FOR THE DEGREE OF
DOCTOR OF PHILOSOPHY

UNIVERSITY OF FLORIDA

1996

To my parents

ACKNOWLEDGMENTS

First, I want to thank Dr. Ramu V. Ramaswamy, my advisor, for his support and guidance throughout the course of this work. His hard work and success in generating funds for the Photonics Research Lab allowed me to complete this work in a very well equipped lab.

I also want to thank Dr. Sheng S. Li, Dr. Arnost Neugroschel, Dr. Ewen Thomson, and Dr. David Tanner for their participation on my supervisory committee.

Thanks also go to my fellow group members in the Photonics Research Lab for their direct or indirect help, particularly, David Maring, Dr. Scott Samson, Mark Skowronski, Dr. Robert Tavlykaev, Dr. Weidong Wang, Dr. Chris Hussell, Dr. Tiziana Conese, Dr. Sanjai Sinha, Dr. Sang-Kook Han and Dr. Hyoon Soo Kim.

I want to thank my parents. They always encourage me to attain higher goals. I know that the progress in my endeavor, such as the completion of this dissertation, is the best expression of gratitude to them.

TABLE OF CONTENTS

	<u>page</u>
ACKNOLEDGMENTS	iii
ABSTRACT	vi
CHAPTERS	
1 INTRODUCTION	1
1.1 Motivation	2
1.2 The Laser-Waveguide Integration Structures	8
1.3 Organization of the Dissertation.. ..	16
2 NOVEL INTEGRATION OF AN SQW LASER AND A TAPERED COUPLER	18
2.1 Multilayer Optical Waveguide.	18
2.2 Quantum Well Lasers	24
2.3 Tapered Waveguide Coupler	30
2.4 The SQW Laser-Waveguide Integration	36
3 MULTIPLE QUANTUM WELL DISORDERING	39
3.1 Introduction	39
3.2 Zn Diffusion Profiles	46
3.3 Compositional Profiles of Disordered MQWs	56
3.4 Refractive Index Profiles of Disordered MQWs	64
3.5 The Optical Confinement Factor	69
3.6 The Lasing Threshold Current Density	77
4 GROOVEBETWEEN THE LASER AND THE TAPER	84
4.1 The Characteristic Matrix	84
4.2 Reflectance of the Groove	88

4.3	The Lasing Threshold Variation	93
4.4	The Power Output Variation	94
5	FABRICATION TECHNIQUES AND EXPERIMENTAL RESULTS.....	98
5.1	Material Growth	98
5.2	MQW Disorder by Zn Implantation and Annealing	101
5.3	Groove Etching By RIE	105
5.4	Fabrication of the Tapered Coupler.....	107
5.5	The Integration	114
6	SUMMARY AND CONCLUSIONS.....	120
	REFERENCES	124
	BIOGRAPHICAL SKETCH	131

Abstract of Dissertation Presented to the Graduate School
of the University of Florida in Partial Fulfillment of the
Requirements for the Degree of Doctor of Philosophy

Integration of a GaAs/AlGaAs SQW Laser and
a tapered waveguide coupler

By

Suning Xie

December 1996

Chairman: Ramu V. Ramaswamy

Major Department: Electrical and Computer Engineering

Future high speed optical fiber communications and signal processing systems require the monolithic integration of a laser source and other passive as well as active devices. Key to integration is the coupling of light from the laser source to a waveguide circuit that make the light available for other optical processing functions such as modulation, switching and routing. Existing integration schemes either require complicated and costly material regrowth or impose severe design and fabrication restrictions. This dissertation studies a novel monolithic integration of a single quantum well (SQW) laser and a tapered waveguide coupler in the GaAs/AlGaAs material system. The integrated structure consists of two sections: the laser and the tapered waveguide coupler. The SQW waveguide for the laser and the multiple quantum well (MQW) waveguide as the output waveguide are vertically stacked. In the laser section, the MQWs are disordered by Zn

implantation and annealing thus becoming the cladding layer of the SQW laser. In the tapered waveguide coupler section, the MQWs are gradually disordered along the waveguide by nitrogen implantation and annealing. This permits the laser output couples to the MQW waveguide for optical processing such as modulation. A groove etched between the laser and the taper sections functions as a partially transmissive mirror providing the feedback for the laser. The tapered waveguide coupler employs an adiabatic power transfer process and allows for independent optimization of individual components to be integrated. The vertical configuration of the two waveguides and the controlled impurity-induced disordering eliminate the regrowth requirements without sacrificing the device design and fabrication flexibility.

In this dissertation, the key technologies for the integration of the SQW laser and the tapered waveguide coupler have been investigated theoretically and experimentally. The MQWs in the laser section are disordered by Zn implantation and subsequent annealing. A finite difference approach has been developed to determine the concentration (Zn) dependent interdiffusion and the model leads to a prediction of a sharp reduction in threshold current density due to the disordering of the MQWs in the laser section, which agreed well with our experimental results. In addition, dependence of the lasing condition due to the groove are investigated. The fabrication techniques including the MQWs disordering by implantation and annealing and the reactive ion etching (RIE) for the groove have been developed. Utilizing these techniques, the integration of an SQW laser and a tapered waveguide coupler in the GaAs/AlGaAs material system has been accomplished.

CHAPTER 1 INTRODUCTION

The breakthrough in semiconductor diode lasers in the 1960s and the development of low loss optical fiber in the 1970s were responsible for the explosion in the fiber optical communication and optical signal processing systems. The progress in these optical systems, in turn, has stimulated the growth of a new class of passive and active optical components in thin dielectric layers using guided wave optics. The highly promising and sophisticated technology responsible for the new class of devices is known as integrated optics. In addition to the advantages of greater bandwidth and immunity from electromagnetic interference, integrated optic devices incorporate increased complex circuitry and functionality along with high reliability. Successful future deployment of optical fiber communications and optical signal processing systems relies on the monolithic integration of a laser source with various passive and active devices. One of the key integrations is the coupling of light from the laser source to a waveguide circuit involving other optical processing such as modulation, switching and routing. In this dissertation, we theoretically and experimentally investigate a novel laser-tapered waveguide coupler integration; in particular, we develop the key fabrication techniques, and demonstrate the monolithic integration in the AlGaAs/GaAs material system. The first section of this introductory chapter

describes the motivation for this work. In section 1.2, we compare various existing laser-waveguide integration structures and introduce the novel structure we proposed. The organization of the remaining chapters of this dissertation is presented in section 1.3.

1.1 Motivation

Optical fiber offers transmission capacity of many orders of magnitude great than that of conventional transmission lines. The overall bandwidth that is available for optical transmission is in the order of THz. This enormous capacity can be accessed by using techniques such as wavelength division multiplex (WDM); it allows for the implementation of many new services such as HDTV distribution, broadband data highways and video telephony. In a WDM system, the overall data stream is divided into a set of sub-streams each having a different wavelength. The optical signals are multiplexed by an optical power combiner and then demultiplexed by optical filters at the receiver ends. Figure 1 shows a multiwavelength optical broadcast network. The network based on the LAMBDANET architecture [1] is composed of a cluster of N communication nodes. Each node transmits its information at a unique wavelength and each node receives all the information from the other nodes. The nodes are optically coupled together using a transmissive optical star coupler at a hub location which broadcasts information at all wavelengths to all nodes.

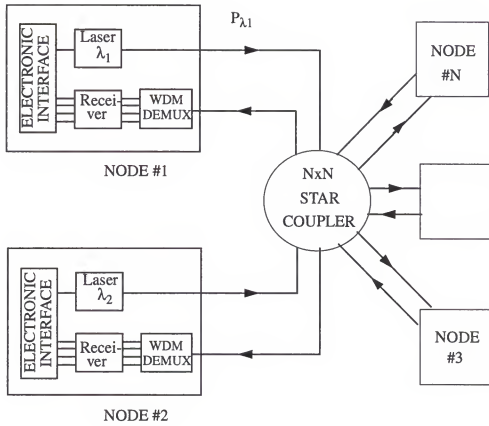


Figure 1.1 The LAMBDANET multiwavelength architecture.

An example of a local video distribution network using the LAMBDANET architecture is shown in Fig. 2 [1]. All the transmitters (lasers) are located in the head end station and all other end stations receive the video broadcast. At least 256 video channels, each at a data rate of approximately 155 Mbit/sec or incorporating time-multiplexed channels within the 155 Mbit/sec stream for even more video channels, are optically multiplexed together to form 16 high speed data channels at 2.5 Gbit/sec, which are transmitted to and demultiplexed at the receiving end stations.

Such a multiwavelength multiplex/demultiplex network demands optoelectronic integration for superior performance and high reliability. Integrated transmitters, receivers, and optical filters are continuously being developed. Transmitters generally include lasers, optical amplifiers, electronic driving/modulation circuits and/or integrated external optical modulators. For wavelength multiplex applications, transmitter arrays are often required. Receiver arrays with on-chip wavelength demultiplexing are desired as well. Integrated receivers employing the polarization diversity coherent detection scheme incorporate a variety of devices including a tunable laser, mode converters, mode splitters, 3 dB couplers, and detectors. Recently a tunable 128 channel optical filter has been demonstrated [2]. This enables transmission of thousands of video channels. Such a highly sophisticated video distribution network can be realized easily with optoelectronic integration, which improves the efficiency and simplifies the packaging as well as alignment of the optical devices.

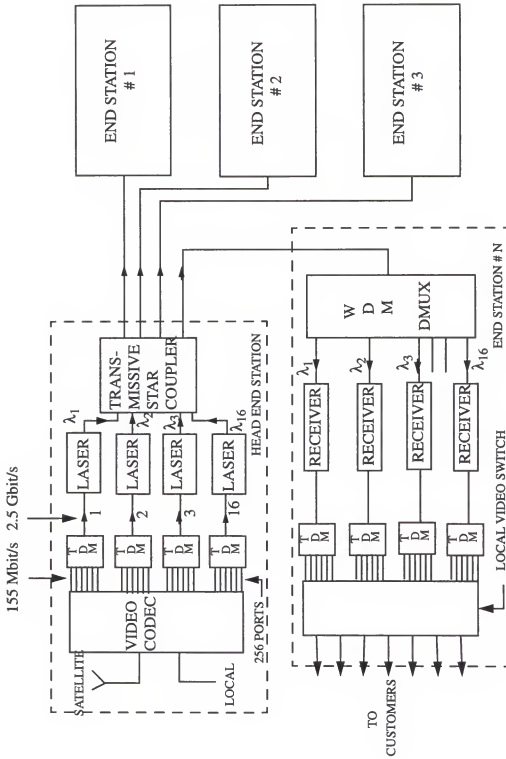


Figure 1.2 A local video distribution network using the LAMBDANET multiwavelength architecture.

One of the key problems in the development of the transmitter is the modulation of the laser. In the example of the video distribution network using a LAMBDANET architecture (Fig. 1.2), 16 channels of 155 Mbit/sec video signals are time-multiplexed together to form a 2.5 Gbit/sec high speed data stream that modulates the laser to generate the optical signals for transmission. High degree of time-multiplexing or other techniques for increasing the number of channels would result in an even higher speed modulation of the laser. However, high speed direct modulation of a semiconductor diode laser causes two problems: dynamic wavelength shift (also known as frequency chirping) and dynamic spectrum broadening.

Direct modulation of a diode laser is performed by modulating the injection current. The modulation of the injection current causes the modulation of the carrier density in the active layer of the diode laser. It is well known that the change in the carrier density results in the change in the refractive index of the active layer due to the change of the band-to-band absorption. A refractive index change in the active layer means a change of the effective optical length in the laser cavity, and therefore results in a shift of the lasing wavelength. This phenomenon is called dynamic wavelength shift, also known as frequency chirping [3-8]. On the other hand, as the carrier density in the active layer oscillates under the modulation, accordingly the medium gain also oscillates in concert. During this process, the mode gains of various longitudinal modes exceed the threshold transiently so that multimode lasing occurs causing dynamic spectral broadening [9-13].

Dynamic wavelength shift and spectral broadening are significant under high speed direct modulation. The wavelength division multiplexing and long distance optical fiber transmission require single wavelength or narrow line width lasers. Dynamic wavelength shift and spectral broadening will reduce the bandwidth of the WDM and optical transmission.

To avoid these shortcomings, an alternative to the direct modulation of the diode laser is to use an external optical modulator. An additional advantage of using an external modulator is that modulators using quantum well effects may have higher modulation speed than direct modulation of the laser diode whose speed is limited by the carrier life time during the recombination.

Monolithic integration of a laser and a modulator has been an active area of research in recent years. Double heterostructure or quantum well lasers and multiple quantum well waveguide modulators have been used in various integration structures [14]. A key problem in the integration is the coupling of the light from the laser to a waveguide to make the light available for modulation. Two factors should be considered in the design of the integrated structure. To make the monolithic integration practical and cost-effective, the fabrication process must be as simple as possible. Among semiconductor processing technologies available today, MOCVD/MBE growth is among the most sophisticated techniques and is quite expensive. Therefore, if possible, regrowth should be avoided in the integrated structure to minimize complexity in fabrication. The optimization of the performance of the integrated structure is another important issue in the design of the

structure. It should be noted in this connection that devices to be integrated on the same chip may have conflicting requirements for layer compositions and dimensions. In view of this, it would be desirable to have an integrated structure that allows for independent optimization of individual components.

This dissertation concentrates on the study of the first part of a laser-modulator transmitter chip, namely, a novel monolithic integration of a single quantum well (SQW) laser and a tapered waveguide coupler. In addition to avoiding the complicated and costly material regrowth, the integration scheme of a SQW laser and a tapered coupler offers flexibility for design and optimization of individual components to be integrated. Its application is not limited to the laser-modulator integration as it also makes the light output from the laser available through a waveguide coupler for other optical signal processing applications such as switching and routing. In the following section, we compare various existing integration structures and introduce the novel structure.

1.2 The Laser-Waveguide Integrated Structures

For the laser-waveguide integration, feedback for the lasing action and coupling of light from the laser to the waveguide must be established in the integrated structure. Conventional semiconductor lasers use cleaved crystal facets as reflectors. Cleaving is a simple procedure and the cleaved facet is flat to an atomic scale. However, it is difficult to apply this technique in a monolithic integrated laser structure. Etched facets and distrib-

uted Bragg reflectors (DBR) are usually used for integrated lasers. Reflectors using etched facets can be fabricated by wet chemical etching or dry etching such as reactive ion etching (RIE). Since the etched facets are defined by the photolithographic processes, they can be made virtually in any shape, size, and crystal orientation and thus a variety of cavities can be fabricated. A distributed Bragg reflector in a semiconductor laser usually has periodic corrugation on the active or passive optical waveguide layer. The equivalent refractive index of the optical waveguide is hence modulated periodically along the waveguide propagation direction so that forward propagating light is scattered backward by Bragg reflection if the wavelength of the light is close to the Bragg wavelength. The periodic corrugations for the distributed Bragg reflector in the semiconductor are generally first patterned by holography or e-beam lithography and then etched by either wet chemical or dry etching. A laser with periodic corrugations on the passive optical waveguides at two ends of the active waveguide is referred to as a distributed Bragg reflector (DBR) laser. A DBR laser is wavelength tunable by the modulation of the refractive index of the distributed Bragg reflector. On the other hand, the periodic corrugation can be fabricated directly on the active optical waveguide to form a distributed feedback laser (DFB). With the advantage of simplicity over DBR lasers, DFB lasers are commonly used for integration.

To date, two types of structures for coupling light from the laser to the waveguide have received widespread use. One is butt-coupling, and the other, directional/evanescent coupling. In a butt-coupling structure, the active waveguide is directly coupled to the output passive waveguide. Usually a DFB laser is used, in which an etched grating on the

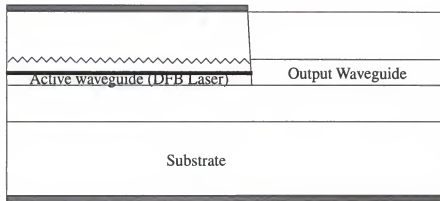
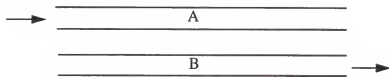


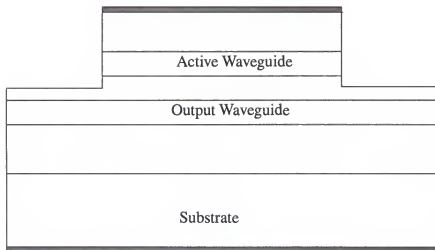
Figure 1.3 DFB laser-waveguide integration using the butt-coupling

active waveguide functioning as a distributed Bragg reflector provides reflection for the lasing action. Figure 1.3 shows a typical butt-coupling scheme [15, 16]. Three growths are required to fabricate such a structure. The lower cladding layer and the active waveguide layers are first grown on the substrate. After the grating is etched over the active waveguide using holography/e-beam lithography and wet/dry etching, a regrowth is performed to form the upper cladding and ohmic contact layers. Generally, the output passive waveguide has material compositions and dimensions different from those of the laser waveguide. To accommodate this requirement, the active waveguide outside the laser portion is etched away and another regrowth needs to be performed to form the passive output waveguide. The main problem with this approach is the cost-effectiveness and the complexity of fabrication. Additionally, the axial offset between the active and passive waveguides must be minimized by accurate control of the etching and regrowth process. When the optimizations of the laser waveguide and the component to be integrated such as a modulator lead to different dimensions in the active and passive waveguides, mode matching and hence the coupling efficiency between the two waveguides may become a significant problem.

In the directional coupling scheme for the laser-waveguide integration, the active and passive waveguides are placed in close proximity so that the mode fields of the individual waveguides overlap. The working principle is the same as that of a directional coupler. When light is launched into one of the two identical waveguides of a directional coupler, generally a symmetric (fundamental) normal mode and an antisymmetric (first



(a)



(b)

Figure 1.4 (a) Directional coupler and (b) Integrated twin guide (ITG) laser using directional coupling.

order) normal mode are excited. The two normal modes are in phase at the input end and the fields of the two normal modes add constructively in the guide A and destructively in the guide B so the light is confined in the input waveguide A. The two normal modes have different propagation constants β_0 and β_1 , respectively. After propagating a distance of the coupling length, the two modes are 180° out of phase and add destructively in the guide A and constructively in the guide B so the power is confined in the guide B. Essentially, the power is transferred from the guide A to the guide B over a distance of the coupling length $l = \pi/(\beta_0 - \beta_1)$. The two individual waveguides may have different refractive indices and dimensions but they must be designed so as to have identical propagation constants at the operating wavelength to achieve complete power transfer between the two guides. Also, the length of the coupling region should be equal to the coupling length which is determined by material compositions and waveguide dimensions.

The integrated twin guide (ITG) laser structure shown in Figure 1.4 employs the directional coupling scheme [17-20]. The laser active waveguide and the passive output waveguide are configured as a vertical directional coupler with light being coupled from the laser waveguide to the output waveguide below. Etched facets in the active waveguide are used as reflectors for the laser. The structure can be fabricated in a single growth. However, due to the interferometric nature of the directional coupler as we discussed above, the two waveguides must have identical propagation constants to achieve efficient coupling. This imposes severe restrictions on the device design and strict tolerance on the fabrica-

tion. Integrated laser structures using directional/evanescent coupling tend to have higher threshold current since the optical field is distributed between the two waveguides resulting in a lower optical confinement factor in the active layer.

To overcome the shortcomings of these structures, recently, a novel monolithic integration of an SQW laser and an MQW modulator via a tapered waveguide interconnect in the AlGaAs/GaAs material system (Figure 1.5) has been proposed and studied in our group [21-23]. The integrated structure consists of three sections: laser, tapered coupler, and modulator. The key technology is the integration of the SQW laser and the tapered waveguide coupler which couples the light from the SQW laser to a MQW waveguide for modulation. In this integrated structure, all layers can be grown in a single growth. Unlike the uniform directional coupler, the tapered coupler employs an adiabatic power transfer process and does not require the two waveguides to have identical propagation constants over the entire length. Somewhat relaxed design constraints and fabrication tolerance as well as the ability to separately optimize individual components provide definite advantages to this approach. In this dissertation, we focus on the study of the monolithic integration of the SQW laser and the tapered waveguide coupler. The integrated structure and its working principles will be discussed in detail in Chapter 2 and key technologies will be further studied in the remaining chapters. The organization of this dissertation is presented in the next section.

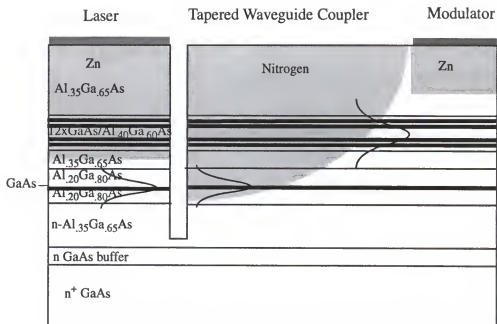


Figure 1.5 A novel monolithic integration of an SQW laser and an MQW modulator via a tapered waveguide coupler.

1.3 Organization of the Dissertation

Following the introduction presented in this chapter, Chapter 2 describes the structure and working principle of the novel monolithic integration of a SQW laser and a taper waveguide coupler. We start with the discussion of multi-layer optical waveguides and quantum well lasers which form the basic components of the integrated structure. Then the principle of the tapered waveguide coupler comprising of a single quantum well (SQW) waveguide and a multiple quantum well (MQW) waveguide will be illustrated. The last section of Chapter 2 discusses the principle of operation, fabrication process, and the advantages of the entire integrated structure.

The key technologies for the fabrication of the novel integrated structure are further studied in the remaining chapters. Three areas of research including the disordering of the MQWs, etched groove, and the fabrication technologies are covered. To achieve low threshold current for the SQW laser, it is necessary to disorder the MQWs in the laser section. In Chapter 3, we numerically model the MQW disordering process by Zn and its influences on the threshold current of the laser. The dependences of the Zn profile, the compositional and refractive index profiles of the disordered MQWs, the optical confinement factor and the laser threshold current on the disordering parameters are calculated. Chapter 4 presents the relations between the reflectance of the groove, the laser threshold current, the output power, and the groove parameters. In Chapter 5, we study the key fabrication technologies including the MQWs disordering by Zn implantation and annealing

and the groove etching by reactive ion etching (RIE). Experimental results are compared with those of the numerical modeling and the integration is demonstrated. In the last chapter, summary and conclusions of this dissertation are presented.

CHAPTER 2

NOVEL INTEGRATION OF A SQW LASER AND A TAPERED COUPLER

This chapter describes and analyzes the novel monolithic integration of a single quantum well (SQW) laser and a tapered waveguide coupler. We first present the basic optical components used in this integration, namely, multiple layer optical waveguide, quantum well laser, and tapered waveguide coupler. Then we describe the integrated structure, its principle of operation, and the techniques employed in fabrication of the structure as well as its advantages over other integrated structures.

2.1 Multilayer Optical Waveguide

The optical waveguides are the building blocks commonly used in both active and passive integrated optic devices where the light is confined and guided in the waveguide. A well known example of the optical waveguides is the optical fiber which has a higher refractive index core surrounded by a low refractive index cladding with usually a circular cross section. Waveguides in integrated optic devices can have planar, channel, ridge and rib structures. Figure 2.1 shows a simple slab planar waveguide which consists of three layers, namely, a substrate, a film, and a cover with refractive indices of n_s , n_f , and n_c ,

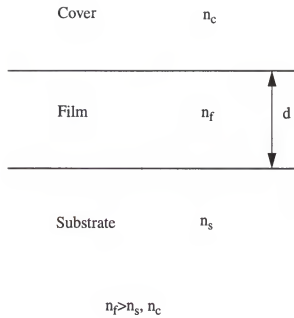


Figure 2.1 A three layer slab waveguide.

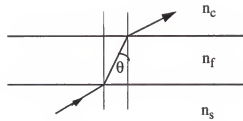
respectively. To guide light in the film, n_f must be greater than n_s and n_c . The cover layer may be air in some devices. The layered structure can be formed by material deposition, diffusion, or epitaxial growth.

A ray optical model of light propagation in this simple waveguide can be used to illustrate the basic concepts of optical waveguides. The underlying principle of guidance in the optical waveguide is the total internal reflection at the interfaces. When light is incident on an interface between two media, reflection and refraction occur. The reflectance and the refractive angles obey Snell's and Fresnel's laws, respectively. If the light is incident on the interface from the higher refractive index (n_f) medium to the lower index (n_s or n_c) medium and the incident angle is greater than the so-called critical angle $\sin^{-1}(n_s/n_f)$, total internal reflection occurs. The amplitude of the reflectance equals one and a phase shift 2ϕ is induced at the interface. The reflectance can be expressed as

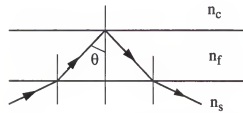
$$r = \exp(j2\phi)$$

The phase shift 2ϕ due to total internal reflection is determined by the incident angle θ and the refractive indices.

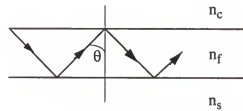
The three layer waveguide shown in Figure 2.1 has two critical angles, θ_s for total reflection at the film-substrate interface and θ_c ($\leq \theta_s$) at the film-cover interface. We assume $n_f > n_s \geq n_c$. When the incident angle θ is smaller than θ_s and θ_c , total reflection does not occur at the two interfaces and the light incident from the substrate is refracted through the film and cover layers and escapes from the guide (Figure 2.2a). There is no confine-



a. True radiation mode



b. Substrate radiation mode



c. Guided mode at discrete angles

Figure 2.2 Modes in the slab waveguide

ment and guiding of the light. This mode of light propagation is called a true radiation mode. When the incident angle is increased such that $\theta_c < \theta < \theta_s$, the total reflection occurs at the film-cover interface but refracted at the film-substrate, as shown in Figure 2.2b. The light again escapes from the guide on the substrate side. This is called a substrate radiation mode. When the incident angle is further increased to $\theta > \theta_s > \theta_c$, total reflection occurs at both interfaces. Under this condition, light entering the film layer may be confined and guided in a zig-zag path in the film (Figure 2.2c) and we have a guided mode.

However, for the guided mode, not all angles of incidence θ are allowed even though they are greater than both critical angles θ_s and θ_c . When the light propagates in a zig-zag path along the waveguide, the total transverse phase shift ϕ_T must satisfy the self-consistency condition (also called the transverse resonance condition), which is $\phi_T = 2v\pi$ ($v=0,1,2,\dots$). The phase shifts in this three layer waveguide include the shift due to a round-trip transverse passage through the film, $2kn_f h \cos\theta$, and shifts due to the total internal reflections at the two interfaces, $-2\phi_s$ and $-2\phi_c$. The self-consistency condition becomes

$$2kn_f h \cos\theta - 2\phi_s - 2\phi_c = 2v\pi$$

where $v=0, 1, 2,\dots$. Note that ϕ_s and ϕ_c are also functions of θ . This condition shows that only a discrete set of angles θ lead to guided modes. The angles with $v=0, 1, 2,\dots$ correspond to the so-called fundamental mode, first-order mode, second-order mode, ..., respectively. From the above equation, it is possible to make the waveguide single-moded (the equation holds only with $v=0$) by properly choosing the values of h , n_f , n_s , and n_c . Once θ_v

is determined from the self-consistency condition, the propagation constants of the guided modes can be calculated from $\beta_v = k n_s \sin \theta_v$. Thus, the self-consistency condition also gives the dispersion relation of the waveguide. This dispersion relation as well as the mode field profiles can also be obtained by using the electromagnetic theory of waveguides.

In practical applications, optical waveguides often have multilayered structures. Semiconductor separate confinement heterostructure (SCH) lasers use a five layer waveguide to achieve separate confinement for the light and the injected carriers[24]. The graded index (GRIN) SCH structure used for single quantum well (SQW) lasers to maximize optical confinement can be treated numerically as a multilayer waveguide[25, 26]. Many guided wave devices that consist of two or more single mode waveguides such as vertical directional couplers can also be considered as a multilayer waveguide. In fact, the two components in our integrated structure, the SQW laser and the tapered coupler, are both constructed from the multilayer waveguide structure. The basic principles for the confinement and guiding of light in a multilayer waveguide are the same as those in a simple three layer waveguide. However, more complicated techniques such as the multilayer stack theory[27] are used to analyze the dispersion relation and field profiles of the guided modes in a multilayer waveguide. An analysis of the tapered coupler as a multilayer waveguide is presented in section 2.3 and the multilayer stack theory is employed in section 3.4 to model the optical confinement dependence of the SQW laser on the MQW disordering.

2.2 Quantum Well Lasers

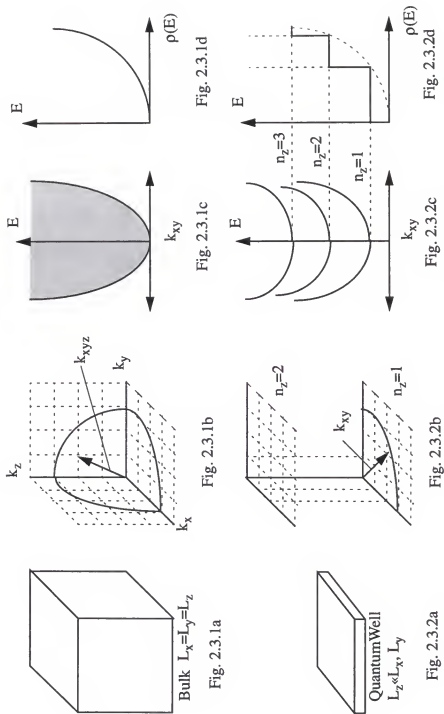
In this section, we review the basics of the quantum well laser which is one of the key components in our integration. Early semiconductor lasers were just a simple GaAs p-n homojunction in a Fabry-Perot cavity formed by two cleaved facets where injected hole and electron carriers recombine and emit photons[28, 29]. The lasing thresholds of these lasers were high and they could operate only in pulsed mode. The development of AlGaAs/GaAs double heterostructure (DH) lasers made the room temperature CW operation possible[30-32]. The bandgap difference between AlGaAs and GaAs provides barriers in the DH structure that confine injected carriers, thus increasing the carrier density. The refractive index difference between the two materials makes the DH structure an optical waveguide that confines the photons increasing the overlap of the optical field and the gain medium. The confinements of the injected carriers and the photons greatly reduce the lasing threshold. The separate confinement heterostructure (SCH) optimizes the confinements of the carriers and photons[33], helps in placing the corrugated grating away from the active layer in the DFB lasers[34] and is a necessity for quantum well lasers in order to maximize the optical confinement.

With their superior in performance, quantum well lasers are now replacing the conventional DH lasers. We begin the comparison of the quantum well and the conventional bulk lasers from the density of states. In a semiconductor crystal, the electronic states in the conduction and valence bands are described by the electron wavefunctions which are

governed by the Schrodinger equation

$$\left[-\frac{\hbar}{2m} \nabla^2 + V(r) \right] \psi = E \psi$$

where $V(r)$ is the potential created by the crystal lattice, ψ is the wavefunction and E the electronic energy associated with the wavefunction. The wavefunctions are uniquely represented by Bloch wave $\psi = e^{ikr} u(k,r)$ and characterized by the electron wavevector k . The fact that the electron wavefunction must go to zero at the edges of the bulk crystal gives the boundary conditions for the wavefunctions resulting in a discrete set of k vectors $k = n_x k_x + n_y k_y + n_z k_z$ where $n_i = 0, \pm 1, \pm 2, \dots$, $|k_i| = \pi/L_i$ and L_i are the crystal dimensions with $i=x, y$, and z . The wavefunctions with these k vectors represent the possible states an electron can have. In III-V semiconductors, the energy E and the k vector of an electron are generally related by $E = E_c + \frac{\hbar^2 k^2}{2m}$, the so-called parabolic band structure approximation. Figure 2.3.1a-c show a cubic bulk crystal, the k vector states in the k space and the energy- k vector relation, respectively. Note that each cross point in the k vector space represents a possible electronic state and the distance between two adjacent points is $|k_i| = \pi/L_i$, which is dependent on the crystal dimensions. If we reduce one of the dimensions L_z ($\ll L_x$ and L_y), the distance between the two adjacent points in the z direction is enlarged and the uniformly distributed k states become far-separated planes of states corresponding to different quantum numbers n_z . Accordingly, the energy is also divided

Figure 2.3 The k state space, E-k, and $\rho(E)$ for bulk crystal and quantum well.

into subbands. These are illustrated in Figure 2.3.2a-c. When L_z is less than 1000 Å for III-V semiconductors, the quantum effect becomes prominent and the structure is called a quantum well. For a quantum well, k_z is many orders of magnitude larger than k_x and k_y . The problem of the density of states becomes two dimensional in each plane and the planes of states in the k space are far apart.

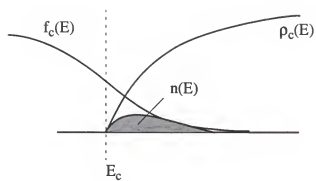
With the help of Figures 2.3.1b and 2.3.2b, the density of states in the k space can be calculated for the bulk and quantum well structures. From the relation between the energy E and the k vector, the density of states in term of energy can be obtained. After extensive and tedious derivations, it can be shown[35] that for the bulk crystal, the density of states $\rho(E)$ is parabolic-like while for the quantum well, $\rho(E)$ is staircase-like discontinuous function with constant density of states at each subband, as shown in Figures 2.3.1d and 2.3.2d, respectively. It should be noted that the staircase-like density of states of a quantum well will reduce to that of the bulk crystal with increasing well thickness.

It is the staircase-like density of states of the quantum well that makes the performances of the quantum well lasers superior to those of the conventional bulk active layer DH laser. Photon emission in a semiconductor laser is the result of the recombination of the injected electrons and hole carriers. The carrier density $n(E)$ is the product of the density of states $\rho(E)$ and the Fermi-Dirac distribution function $f(E)$ which determines the probability of an carrier occupying an energy level E and is expressed as

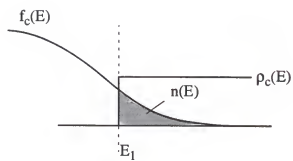
$$f(E) = \frac{1}{1 + \exp[(E - E_f)/(k_B T)]}$$

where E_f is the quasi-Fermi level determined by the total number of injected carriers. The $\rho(E)$, $f(E)$ and $n(E)$ for the bulk crystal and the quantum well are plotted in Figures 2.4a and 2.4b, respectively. The differences in the carrier density profiles as a result of the different densities of states lead to different responses to the increase in the total number of injected carriers. In the bulk crystal, the carrier density as a function of energy increases gradually since the density of states increases with increasing energy. It reaches a maximum and then decreases because the electrons have lower probability of occupying higher energy levels as the Fermi-Dirac distribution decreases with increasing energy. For the quantum well, because of the constant value of the density of states, electrons occupy the bandedge immediately with the peak of the carrier density located at the bandedge with a narrower width. This leads to a much larger increase in the bandedge carrier density in response to the increase of the total number of injected carriers which corresponds to a shift of the Fermi level to a higher energy level. The enhancement of the bandedge carrier density greatly increases the peak gain making a low lasing threshold possible. It should be noted that with a quantum wire structure, the density of states decreases with increasing energy level and the bandedge carrier density will be further enhanced.

With the advances in the epitaxial growth technology, the quantum well lasers were demonstrated experimentally and their advantages exemplified [36-38]. For the GaAs/ $\text{Al}_x\text{Ga}_{1-x}\text{As}$ material system, AlGaAs that has a larger bandgap is used as the barrier while a lower bandgap GaAs or low Al concentration (small x) AlGaAs layer, sandwiched



a. bulk



b. quantum well

Figure 2.4 schematic plots of $n(E)$, $r(E)$ and $f(E)$.

between two barrier layers, acts as the quantum well. Typically, the well thickness is below 100 \AA . Such a thin layer of high quality can be grown either by molecular beam epitaxy (MBE) or by metal organic chemical vapor deposition (MOCVD). For quantum well lasers, it is necessary to use a separate confinement heterostructure (SCH) to improve the optical confinement in the active well layer. Step index or graded index (GRIN) SCH is employed to form an optical waveguide in order to confine the lasing light [39]. In Section 3.5, we will investigate the dependence of the SQW laser threshold current on the MQW disordering parameters.

2.3 Tapered Waveguide Coupler

Tapered directional coupler is another key component in the laser-waveguide integration. It couples the SQW laser waveguide to the MQW output waveguide. Although the structure of a tapered coupler is similar to that of a conventional directional coupler, its principle of operation is completely different. Figure 2.5 shows a tapered directional coupler that consists of two planar waveguides with the top guide thickness tapered. Curves labeled a and b in Figure 2.5 represent the propagation constants of the two individual waveguides. The two modes are synchronous at the center of the coupler where the two waveguides have identical thicknesses. The power transfer between the two waveguides can be analyzed using the concept of local normal modes. We mentioned in Section 2.1 that the structure of a two-guide coupler can be viewed as a multilayer waveguide. In this

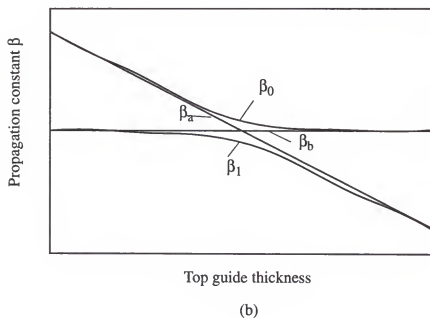
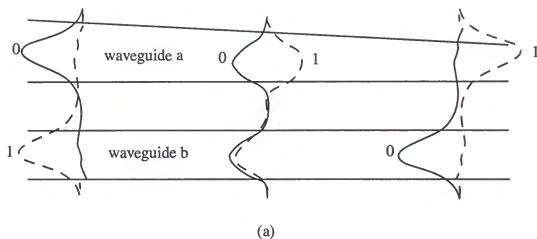


Figure 2.5 (a) A tapered directional coupler with top guide thickness tapered. (b) Propagation constants of the modes of individual guides β_a and β_b and local normal modes β_0 and β_1 of the composite structure.

case, the composite structure is a five layer waveguide. Since the waveguide is tapered, the mode characteristics will vary along the five-layer waveguide and therefore, we must deal with the local normal modes. The local normal modes are the normal modes of the five layer waveguide at a given position along its length. Using the multilayer stack theory [27], the propagation constants β_0 and β_1 and corresponding field profiles of the local normal modes as a function of the position can be calculated. The β_0 and β_1 are illustrated in Figure 2.5 and the field profiles as a function of the positions along the length of the slowly varying taper are also shown in the figure. Note that at the input end of the coupler, the fundamental mode (β_0) has its power concentrated in the upper guide and at the output end, the power is concentrated in the lower guide. For the first order mode (β_1), the power shifts from the lower guide to the upper guide. Essentially, due to the gradual tapering, the normal modes evolve slowly along the coupler altering the field profiles and resulting in power transfer between the two waveguides. If we excite only one normal mode in the coupler, we would expect to achieve a complete power transfer from one guide to the other. However, an important condition must be met. The mode propagation along the tapered coupler can be analyzed using the step transition model [40, 41] in which the continuously tapered structure is approximated by a series of discontinuous, abrupt steps. Since the local normal modes in two adjacent steps are not orthogonal, coupling between them can occur at each step meaning the power in the fundamental mode can be coupled into the first order mode in the next step. This would cause large crosstalk in the coupler.

However, if the tapering of the waveguide is sufficiently gradual, the coupling between the two local normal modes is negligible and the power will remain in one mode and transform itself from being concentrated in one guide to being concentrated in the other. This is the adiabatic operation. An analysis [41] using the step transition model yields three conditions for the tapered coupler:

$$1) \frac{(\Delta\beta_T)/(\Delta Z_T)}{\kappa\kappa^*} \leq 1.5 \text{ for adiabatic operation,} \quad (2.1)$$

$$2) \Delta Z_T \geq 213/(\Delta\beta_T) \text{ for complete power transfer (>95\%),} \quad (2.2)$$

and

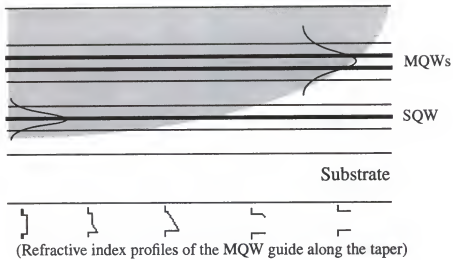
$$3) \text{ large } (\Delta\beta)/|\kappa| \text{ ensuring only one local normal mode is excited by power launched into one guide,} \quad (2.3)$$

where $\Delta\beta_T$ is the total variation of the difference in the propagation constants of the tapered guide over the taper length ΔZ_T , and κ is the coupling coefficient between the two individual guides.

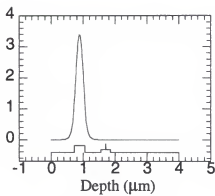
These conditions show the advantages of the tapered couplers over the conventional directional couplers. Recall our brief discussion of the latter in Section 1.2. The normal mode field profiles do not change when the modes propagate along the conventional coupler because it uses two uniform waveguides. The power transfer is due to the constructive or destructive interference of the symmetric and antisymmetric normal modes instead of the evolution of a single quasi-normal mode. This interferometric nature of the

coupler requires two synchronized waveguides with exact device length (equal to the coupling length) to achieve efficient power transfer, thus imposing severe design and fabrication restrictions. On the contrary, conditions for the tapered coupler (Eqs. 2.1-2.3) are all inequalities and can be satisfied by a wide range of parameters.

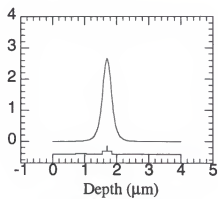
The tapered directional coupler used in our integration is somewhat more complicated (Figure 2.6). The lower waveguide is an SQW separate confinement heterostructure (SCH) while the guiding layer of the upper waveguide is an MQW structure. The tapering of the coupler is realized by gradually disordering the MQWs along the coupler instead of changing the guide thickness. The disordering of the quantum wells alters the refractive index profiles which are shown schematically in representative positions along the coupler in Figure 2.6. The coupler is designed in such a way that the light launched into the SQW waveguide excites only the fundamental mode whose power is concentrated in the SQW guide at the input end and the mode evolves adiabatically along the tapered coupler with the power eventually transferred and concentrated in the MQW guide at the output end [42]. The field profiles of the normal modes are also shown in Figure 2.6. At the input end where MQWs are completely disordered, the fundamental mode field is concentrated in the SQW waveguide while at the output end with undisordered MQWs, the field is concentrated in the MQW waveguide. The fabrication of the tapered coupler using Zn, F, O₂ and N₂ disordered MQWs have been investigated in our group [43]. Its advantages, appli-



Structure



a) Disordered region



b) Undisordered region

Field profile

Figure 2.6 The tapered waveguide coupler.

cation and fabrication in the laser-waveguide integration will be discussed in the next section.

2.4 The SQW laser-MQW waveguide Integration

In the previous sections, we analyzed the principles of the key components in the integration of an SQW laser and a tapered waveguide coupler. Figure 2.7 shows the proposed integrated structure. The multilayer structure can be grown in a single growth. A 0.5 μm thick, n--type doped GaAs buffer layer is first grown on the n^+ GaAs substrate, followed by an 1.5 μm thick, n^- $\text{Al}_{0.35}\text{Ga}_{0.65}\text{As}$ lower cladding layer for the SQW waveguide. Then, a 0.15 μm $\text{Al}_{0.20}\text{Ga}_{0.80}\text{As}$ lower guiding layer, a 90 \AA GaAs quantum well layer, and again a 0.15 μm $\text{Al}_{0.20}\text{Ga}_{0.80}\text{As}$ upper guiding layer, all undoped, are grown. After growth of a 0.5 μm , undoped $\text{Al}_{0.35}\text{Ga}_{0.65}\text{As}$ cladding layer, 12 periods of 65 \AA GaAs/190 \AA $\text{Al}_{0.40}\text{Ga}_{0.60}\text{As}$ quantum well/barrier layers are grown to form the MQW waveguide. Finally, a 0.7 μm thick $\text{Al}_{0.35}\text{Ga}_{0.65}\text{As}$ cladding layer and a 250 \AA GaAs cap layer, both undoped, are grown. In this structure, the SQW and MQW waveguides are vertically stacked. In the laser section, the MQWs are completely disordered by Zn implantation and annealing, thus, becoming the cladding layer of the SQW laser waveguide. In the coupler section, quantum wells are gradually disordered along the waveguide by Nitrogen implantation and annealing forming a tapered directional coupler. A groove etched between the

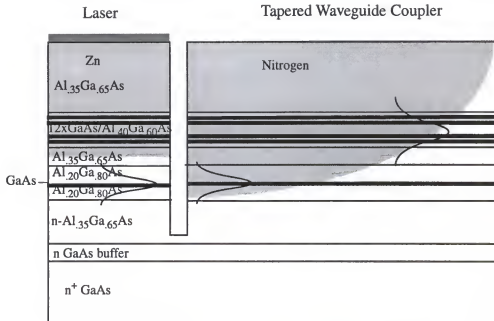


Figure 2.7 Monolithic integration of a SQW laser and a tapered waveguide coupler.

laser section and the tapered coupler functions as a partially transmissive mirror for laser feedback. In this structure, light from the laser is launched into the SQW waveguide through the etched groove and coupled into the output MQW waveguide by another passive, tapered, adiabatic coupler.

Such a structure has unique advantages. As we pointed out in Section 2.3, the tapered directional coupler employs an adiabatic power transfer process and can be realized by using a wide range of device parameters such as dimensions and layer compositions for the two waveguides instead of a set of discrete parameters dictated by the interferometric nature of the conventional directional coupler. This allows for independent optimization of individual components. For example, we used an SQW SCH waveguide for the laser and an MQWs structure as the output waveguide for modulation. Moreover, the vertical configuration of the two waveguides eliminates the requirements for complicated and costly material regrowth without sacrificing the design and fabrication flexibilities.

In the following chapters, we investigate the key concepts and technologies required for the SQW laser-MQW waveguide integration viz., Zn disordering of the MQWs, etched groove and their influence on the threshold of the SQW laser, and the associated fabrication techniques.

CHAPTER 3

MULTIPLE QUANTUM WELL DISORDERING

3.1 Introduction

The laser section in the laser-coupler integration consists of a vertically stacked single quantum well (SQW) waveguide and a multiple quantum well (MQWs) region. The multiple quantum wells form an optical waveguide in the tapered coupler section and are completely disordered in the laser section thus becoming a part of the cladding layer for the SQW laser waveguide. The complete disordering is necessary to reduce the threshold current of the SQW laser. The characteristic of low lasing threshold due to the quantum effect in quantum well lasers is compromised by the fact that the quantum well active layer that confines the injected carriers is so thin ($\sim 100 \text{ \AA}$) that it provides little confinement for the emitted photons. For optical confinement, the double heterostructure (DH) should have an appropriate refractive index difference and a thickness on the order of the optical wavelength, which is typically several thousand \AA for the GaAs/AlGaAs material system. Generally, a separate confinement heterostructure (SCH) is used to improve the optical confinement in quantum well lasers. Figure 3.1 shows the Al compositional profiles of step index and graded index (GRIN) SCH SQW lasers. The thin GaAs quantum

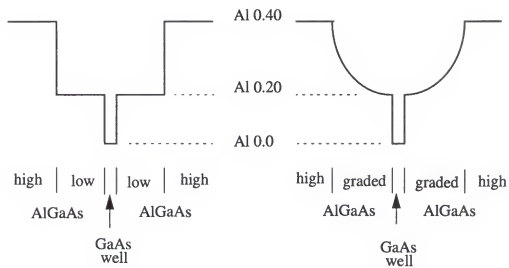


Figure 3.1 Step index and graded index separate confinement heterostructures (SCH)

well active layer is sandwiched between two thin, low Al concentration AlGaAs layers that serve as the barrier for the quantum well as well as the guiding layer. In addition, these are surrounded by two thick, high Al concentration, lower refractive index AlGaAs cladding layers that provide the optical confinement.

The lasing condition can be expressed as

$$\Gamma g_{th} = \alpha_i + \frac{1}{2L} \ln \frac{1}{r_1 r_2}$$

where

$$\Gamma = \frac{\int_a^\infty |E|^2 da}{\int_{-\infty}^\infty |E|^2 da}$$

is the optical confinement factor in the active layer a and E is the optical field profile. α_i is the internal loss coefficient in the laser cavity with the length L , and r_1 and r_2 are the reflectivities of the two facet mirrors. The threshold gain g_{th} determines the threshold current density. Higher the threshold gain, higher the threshold current density. α_i , r_1 and r_2 are mainly determined by the materials of the gain medium and end facets. This relation shows a large optical confinement factor Γ will result in a low threshold current density. Physically, the more the optical field is concentrated in the SQW active layer, the lower the threshold current density as more of the generated light experiences the gain in the cavity. The field profile and the optical confinement factor is determined by the refractive index

profile of the structure. Figure 3.2 shows the compositions and thicknesses of the vertically stacked MQW-SQW structure under investigation. Its refractive index and field profiles are illustrated in Figure 3.3. Note that the undisordered MQWs region has a high refractive index and the disordering of the MQWs reduces its refractive index. Without the disordering, the MQWs region itself is a waveguide next to the SQW waveguide and the field of the fundamental mode of the composite SQW/MQW structure is confined in the MQWs region, as shown in Figure 3.3a, resulting in a nearly zero confinement of the light in the SQW active layer of the laser. Disordering of the MQWs modifies the refractive index profile affecting the field profile and hence the optical confinement factor. Only when the MQWs are completely disordered will the optical field be well confined in the SQW waveguide (Figure 3.3b). In this case, the SQW laser exhibits the maximum confinement factor and lowest threshold current density.

Disordering the MQWs in the laser section is a better way to modify the refractive index profile than removing the MQWs by etching. The latter approach leaves a very thin cladding layer for the SQW laser with the metal electrode over it. The field penetrating into the metal as well as high doping cladding layer for ohmic contact would result in a higher loss and a higher lasing threshold. The disordering of the quantum well is performed by introducing impurities into the quantum well at high temperature. The GaAs/AlGaAs heterostructures are in general very stable. Thermal anneal below 800 °C causes little intermixing. However, the situation is completely different when impurities are introduced in the structure. Total intermixing i.e., impurity induced disordering may occur

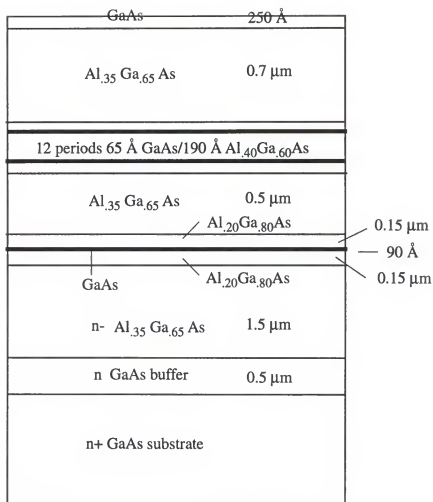
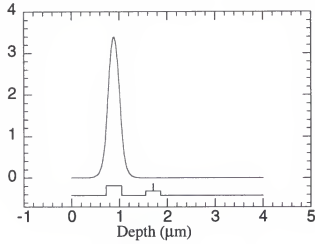
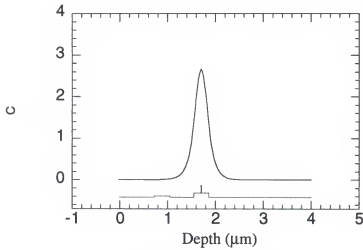


Figure 3.2 The layer compositions and thicknesses of the SQW/MQW structure under investigation.



a) MQWs not disordered



b) MQWs disordered

Figure 3.3 Refractive index and fundamental mode field profiles of the SQW/MQW structure with the undisordered (a) and disordered (b) MQWs.

resulting in the GaAs/AlGaAs quantum well becoming an AlGaAs alloy, whose Al composition is the average of the layers.

In this chapter, we investigate analytically the dependence of the lasing threshold on the disordering parameters. We will compare the calculations with the experimental results in Chapter 5. The layer compositions and thicknesses of the SQW/MQW structure under consideration for the SQW laser - coupler integration is illustrated in Figure 3.2. We use zinc to disorder the quantum wells as zinc also functions as p-type dopant for the p-n junction and ohmic contact. Zinc is implanted into the sample and then annealed. The degree of disordering depends on the Zn concentration. In Section 3.2, first, we determine the Zn profile due to annealing by solving Fick's second law with a concentration dependent diffusion coefficient using finite difference method (FDM). In Section 3.3, with Zn concentration in the MQWs region as a function of the annealing time and position, the coefficient of Zn induced Al and Ga interdiffusion between the quantum well and barrier are determined and we develop a finite difference approach using the Crank and Nicholson method to obtain the compositional profile of the disordered MQWs. The equivalent refractive indices of the disordered MQWs are then calculated by solving the Schrodinger equation using the FDM in Section 3.4. In Section 3.5, using the disordering modified refractive index profiles, the optical confinement factor in the laser active layer is then calculated with the help of the multilayer stack theory. Finally in Section 3.6, the laser threshold dependence on the MQW disordering is investigated.

3.2 Zn Diffusion Profiles

The degree of the MQWs disordering depends on the Zn concentration. In this section, we model the Zn profile due to annealing. Generally, diffusion is the result of a concentration gradient of mobile atoms. The flux of the moving atoms is proportional to the negative concentration gradient and expressed by Fick's law as

$$J = -D\nabla C$$

where J is the flux of the diffusing atoms, C is the concentration, and D is the proportional constant, termed as the diffusion coefficient. By applying the continuity condition that the rate of change of concentration in a given volume, $\frac{\partial C}{\partial t} \Delta x \Delta y \Delta z$, must equal the net divergence of the flux of the atoms flowing in and out to the volume, $-\nabla \cdot J \Delta x \Delta y \Delta z$, we get

$$\frac{\partial C}{\partial t} = -\nabla \cdot J.$$

Using Fick's law and assuming the diffusion coefficient D is constant, we obtain Fick's second law

$$\frac{\partial C}{\partial t} = D\nabla^2 C. \quad (3.1)$$

With the boundary and initial conditions, the diffusion profile can be obtained by solving the above equation either analytically or numerically.

Fick's second law applies to most common diffusions in which the diffusion coefficient remains constant. However, Zn diffusion in GaAs/AlGaAs is more complicated and does not have a constant diffusion coefficient. A substitutional-interstitial diffusion mechanism has been suggested to explain this diffusion[44-47]. Zn, a group II element, generally occupies substitutionally the sites of group III element Ga, in GaAs, acting as a singly ionized acceptor s^- whose concentration is S . At the same time, a small portion of Zn exists interstitially, acting as a singly ionized donor i^+ with concentration I . The diffusion coefficient of the substitutional Zn is negligible and Zn diffusion is due to the movement of the highly mobile interstitial Zn. The transition of Zn between the substitutional and interstitial forms are expressed as



where h represents holes with a concentration of p and v_{III} the vacancies on the Ga sites with concentration V assumed constant. At equilibrium, the law of mass action leads to

$$K_1 p^2 S = IV.$$

By postulate, $S \gg I$ so we have $p \approx S$ for the material to be neutral. Thus,

$$K_1 S^3 = IV.$$

On the other hand, since the change of the total concentration ($S+I$) is due to the diffusion of the interstitials, we have

$$\frac{\partial S}{\partial t} + \frac{\partial I}{\partial t} = D_i \frac{\partial^2 I}{\partial x^2}$$

where D_i is the diffusion coefficient of the interstitials. Substituting for I using the last equation, we obtain

$$\frac{\partial S}{\partial t} = \frac{\partial}{\partial x} \left(D \frac{\partial S}{\partial x} \right) \quad (3.2)$$

with

$$D = \frac{3K_1 D_i S^2}{V}.$$

Since $S \gg I$, in effect, the total concentration $C \approx S$. Therefore, for Zn diffusion in GaAs/AlGaAs, we have a diffusion equation in the form of Fick's second law but with a concentration dependent diffusion coefficient, $D = D_0 C^2$.

Solving the Zn diffusion equation for the impurity profile in the SQW/MQW structure is further complicated by the fact that the medium is a multilayer heterostructure. Since no closed form analytical solution is available, we use a finite difference method (FDM). The diffusion equation is approximated by a group of finite difference equations that relate the concentration at a point to those at the neighboring points and then solved subject to the boundary and initial conditions. The approximations are based on

$$\frac{\partial}{\partial x} C(x_0, t) \approx \frac{C(x_0 + \Delta x, t) - C(x_0, t)}{\Delta x}, \quad (3.3)$$

$$\frac{\partial^2}{\partial x^2} C(x_0, t) \approx \frac{C(x_0 + \Delta x, t) - 2C(x_0, t) + C(x_0 - \Delta x, t)}{2\Delta x} \quad (3.4)$$

and

$$\frac{\partial}{\partial t} C(x, t_0) \approx \frac{C(x, t_0 + \Delta t) - C(x, t_0)}{\Delta t} . \quad (3.5)$$

In the FDM, the x - t plane, where x is the distance coordinate along the diffusion direction and t is the diffusion time, is divided into a grid of nodes with each node represented by a pair of numbers (i, j) , as show in Figure 3.4. Thus, Equations (3.3), (3.4) and (3.5) can be expressed as

$$\left. \frac{\partial C}{\partial x} \right|_{i,j} \approx \frac{C_{i+1,j} - C_{i,j}}{\Delta x} \quad (3.6)$$

$$\left. \frac{\partial^2 C}{\partial x^2} \right|_{i,j} \approx \frac{C_{i+1,j} - 2C_{i,j} + C_{i-1,j}}{(\Delta x)^2} \quad (3.7)$$

and

$$\left. \frac{\partial C}{\partial t} \right|_{i,j} \approx \frac{C_{i,j+1} - C_{i,j}}{\Delta t} . \quad (3.8)$$

The notation of i and j is convenient for computer simulation, especially when adaptive meshes are used. For homogeneous materials, substitution of Equations (3.6), (3.7) and (3.8) into Fick's second law lead to algebraic finite difference equations that can be solved for diffusion profiles.

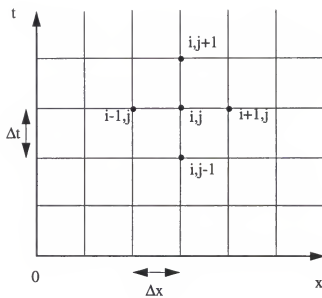


Figure 3.4 Finite difference mesh for the diffusion equation.

For our SQW/MQW multilayer heterostructure, the interface problem should be considered. For efficient computing, use of adaptive meshes is desired. We derive a set of general finite difference equations that use adaptive meshes and apply to both the points in the volume and at the interfaces. The Zn diffusion equation (3.2) becomes

$$\frac{\partial C}{\partial t} = \frac{\partial}{\partial x} \left(D \frac{\partial C}{\partial x} \right) = D \frac{\partial^2 C}{\partial x^2} + \frac{\partial D}{\partial x} \frac{\partial C}{\partial x}. \quad (3.9)$$

We consider an interface, located at the coordinate i , between two media with diffusion coefficients D_a and D_b , respectively, as shown in Figure 3.5a. At the interface, the continuity condition requires that the flux of diffusing atoms be continuous; therefore,

$$D_a \frac{\partial C_a}{\partial x} \Big|_i = D_b \frac{\partial C_b}{\partial x} \Big|_i = F. \quad (3.10)$$

For finite difference expressions, we extend medium a one step Δx_a to the right of the interface and introduce a 'fictitious' concentration $C_{a+i,j}$ (Figure 3.5b). Using (3.3), the left-hand side of Equation (3.10) can be expressed as

$$D_a \frac{C_{a+i,j} - C_{a-i,j}}{2\Delta x_a} = F. \quad (3.11)$$

Also,

$$\frac{\partial^2 C_a}{\partial x^2} \Big|_i = \frac{C_{a+i,j} - 2C_{a,j} + C_{a-i,j}}{(\Delta x_a)^2} \quad (3.12)$$

Eliminating $C_{a+i,j}$ in (3.12) by using (3.11) and substituting into (3.9), we have

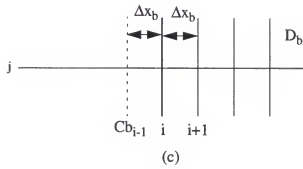
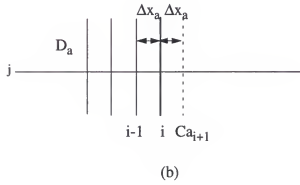
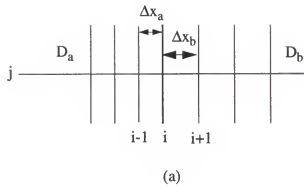


Figure 3.5 Finite difference mesh at the interface i

$$\frac{\partial C_{i,j}}{\partial t} = \frac{2D_a}{\Delta x_a} \left(\frac{C_{i-1,j} - C_{i,j}}{\Delta x_a} + \frac{F}{D_a} \right) + \frac{\partial D_a}{\partial x} \frac{\partial C_{i,j}}{\partial x}. \quad (3.13)$$

Similarly, using a 'fictitious' concentration $C_{b-i,j}$ (Figure 3.5c), we have

$$\frac{\partial C_{i,j}}{\partial t} = \frac{2D_b}{\Delta x_b} \left(\frac{C_{i+1,j} - C_{i,j}}{\Delta x_b} + \frac{F}{D_b} \right) + \frac{\partial D_b}{\partial x} \frac{\partial C_{i,j}}{\partial x} \quad (3.14)$$

Eliminating F from (3.12) and (3.13) and using (3.7) and (3.5), we obtain the finite difference expression of the diffusion equation

$$\begin{aligned} C_{i,j+1} = C_{i,j} &+ \frac{2\Delta t}{\Delta x_a + \Delta x_b} \left(\frac{D_a}{\Delta x_a} (C_{i-1,j} - C_{i,j}) + \frac{D_b}{\Delta x_b} (C_{i+1,j} - C_{i,j}) \right. \\ &\left. + D_{a0} C_{i,j} \frac{(C_{i,j} - C_{i-1,j})^2}{\Delta x_a} + D_{b0} C_{i,j} \frac{(C_{i+1,j} - C_{i,j})^2}{\Delta x_b} \right) \end{aligned} \quad (3.15)$$

Therefore, the concentration at point i and time $j+1$ can be calculated from the concentrations of neighboring points $i-1$, i , and $i+1$ at a previous time j . Note that for homogeneous materials with non-concentration dependent diffusion coefficient ($D_a=D_b=\text{constant}$) and constant mesh size ($\Delta x_a=\Delta x_b$), the above equation reduces to the conventional form of finite difference equation [48]

$$C_{i,j+1} = C_{i,j} + \frac{\Delta t D}{(\Delta x)^2} (C_{i+1,j} - 2C_{i,j} + C_{i-1,j}).$$

In the laser section of the integrated structure, Zn is first implanted into the sample and then annealed. The advantage of Zn implantation over diffusion by Zn vapor or deposited metallic Zn is that the implant dosage of Zn can be easily controlled. When the anneal

temperature and time are fixed, the level of Zn concentration in the MQW region determines the degree of the MQW disordering since the impurity induced interdiffusion coefficient is a function of Zn concentration. In the calculation, we use an anneal time of 40 minutes and a temperature of 700 °C. We assume the Zn diffusion coefficient $D(x) = D_0(C(x)/1 \times 10^{19})^2$, where D_0 is extracted from references 49 and 50 for various material compositions as follows: GaAs 1×10^{-14} cm²/s, Al_{0.35}Ga_{0.65}As 1×10^{-13} cm²/s, the MQW 5×10^{-14} cm²/s, Al_{0.2}Ga_{0.8}As 8×10^{-14} cm²/s. For the MQWs, an equivalent diffusion coefficient is used. The initial depth of the implanted Zn is 0.35 μm. The layer thicknesses of the MQW/SQW structure under consideration are shown in Figure 3.3. Figure 3.6 shows the calculated Zn profiles after annealing with various initial Zn concentrations. Note that the diffusion fronts are all abrupt, which is the typical characteristic of Zn diffusion in III-V semiconductors. Since the diffusion coefficient increases with the Zn concentration, the diffusion depth increases with the initial Zn concentration. The calculated Zn profile data as a function of depth and time are saved for the numerical modeling of the MQW disordering in the next section.

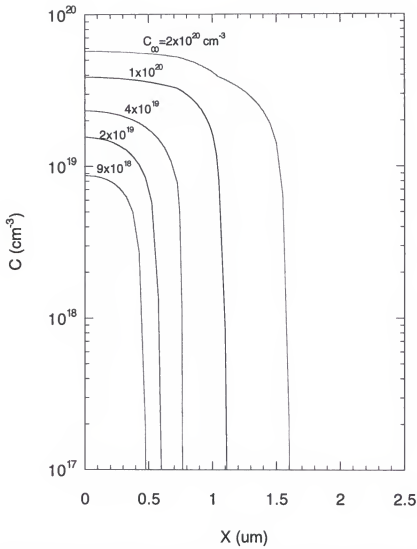


Figure 3.6 Calculated Zn profiles in the GaAs/AlGaAs MQWs/SQW structure after annealing with various implanted Zn concentrations C_{00} .

3.3 Compositional Profiles of Disordered MQWs

We introduced the impurity induced disordering of quantum wells in the first section (3.1) of this chapter. In this section, we discuss the mechanism of the disordering and model the compositional profiles of the disordered multiple quantum wells due to the Zn diffusion, discussed in the previous section. The results will be used to investigate the dependence of the lasing threshold on the disordering parameters in the later sections. The impurity induced disordering was discovered in early 1980s [51, 52]. Several mechanisms have been proposed to explain the Zn diffusion induced disordering including the Zn vacancy pair mechanism [51], the single vacancy ring and divacancy ring mechanism [53], the As antisite defect mediated mechanism [54], the mechanism involving Coulombic interactions between substitutional impurity atoms and host atoms [55], and the self-interstitial mechanism [56-59]. The self-interstitial mechanism has been widely accepted. We discussed in Section 3.2 that Zn diffuses in GaAs/AlGaAs via the substitutional-interstitial mechanism. Zn atoms move as interstitial donors and then occupy group III vacancy sites becoming immobile substitutional acceptors. The group III vacancies are generated by Zn interstitials via a 'kick-out' mechanism in which group III atoms Ga and Al become interstitial and their sites become vacancies. Similar to the diffusion of Zn, Ga and Al on their sites have negligible diffusion coefficient so the interdiffusion, or intermixing, of Ga and Al between the quantum well and barrier layer is negligible. However, when Zn is diffused

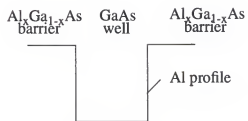
into the crystal, interstitial Ga and Al are generated via the kick-out mechanism. Like Zn interstitials, these interstitials also have large diffusion coefficients. Because of the concentration difference between the GaAs well (low Al and high Ga) and the AlGaAs barriers (high Al and low Ga), the Al interstitials in the barrier layers will diffuse into the well layers and the Ga interstitials in the well layer diffuse into the barrier layers, leading to a layer disordering (Figure 3.7). It is these Zn diffusion generated Al and Ga interstitials that enhance the interdiffusion between the layers.

Fick's second law (3.1) can be applied to the Al and Ga interdiffusion between the quantum well and barrier layers since it is a diffusion of interstitials. It is generally accepted that the diffusion coefficients for Al in GaAs and Ga in AlGaAs are very close [59]. The interdiffusion coefficient

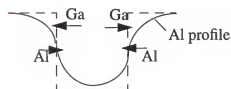
$$D_i \approx D_{Al}^{GaAs} \approx D_{Ga}^{AlGaAs}$$

where D_{Al}^{GaAs} and D_{Ga}^{AlGaAs} are the diffusion coefficients of Al in the GaAs well and Ga in the AlGaAs barriers, respectively. It should be noted that the interdiffusion coefficient is Zn concentration dependent according to the self-interstitial mechanism. It varies with the disordering time since the interdiffusion proceeds at the same time as the Zinc diffusion.

Two approaches have been used to model the Zn induced disordering in the GaAs/AlGaAs quantum wells. The first approach uses the Boltzmann-Matano technique [60]. This approach basically transforms the two-variable diffusion equation complicated by the



a. Before disordering



b. Partially disordered

Figure 3.7 Illustration of the disordering of a GaAs/AlGaAs quantum well.

concentration dependent diffusion coefficient into a single-variable equation. This technique requires that the boundary conditions can be described in term of the new variable, which restricts the application of this technique in many cases. Moreover, the requirement that the diffusion coefficient is a function of concentration only, is a major problem when using this approach for the disordering process. As discussed earlier in this section, the interdiffusion coefficient varies with time. Several researchers used this technique to obtain information on the disordering [59, 61]. It has been pointed out [62] that the Boltzmann-Matano analysis does not apply in the case of disordering due to the time variance of the interdiffusion coefficient.

Another approach uses an error function approximation [63, 64]. The Al composition profile of the disordered quantum well is approximated by

$$x(z) = x_0 \left[1 + \frac{1}{2} \operatorname{erf} \left(\frac{z - L_z/2}{2\sqrt{Dt}} \right) - \frac{1}{2} \operatorname{erf} \left(\frac{z + L_z/2}{2\sqrt{Dt}} \right) \right]$$

where x_0 is the Al concentration of the AlGaAs barrier before the disordering, L_z is the well thickness, D the interdiffusion coefficient, and t the interdiffusion time. Again, this approach ignores the time dependence of the interdiffusion coefficient. The assumption for this approximation is that the barrier thickness is infinite, which is not the case for multiple quantum wells and superlattices. Moreover, for slight disordering, the error function is a poor approximation.

We develop a finite difference approach with a Zn-concentration and time dependent interdiffusion coefficient. The diffusion equation from (3.1) for Al is

$$\frac{\partial}{\partial t}x(z, t) = D(C_{Zn}, t)\frac{\partial^2}{\partial z^2}x(z, t) \quad (3.16)$$

where $x(z, t)$ is the Al concentration at the position z and time t , $D(C_{Zn}, t)$ the interdiffusion coefficient with Zn concentration C_{Zn} at time t . Using similar arguments for the Zn diffusion, we can obtain an explicit finite difference expression of the diffusion equation identical to Equation (3.15) except that the last two non-linear terms are dropped because the interdiffusion coefficient $D(C_{Zn}, t)$ is not a function of the Al concentration x .

However, the explicit expression (3.15) does not always give stable and converging solutions. Care must be taken of the choice of the mesh sizes. In order to ensure a stable solution and reduce error, we derive an implicit finite difference expression using the Crank and Nicholson formula [65]. When deriving the explicit expression, values of $x(z, t)$ at time j and $j+1$ were used for the term on the left hand side of Equation (3.16) while values at time j were taken for the terms on the right hand side. Crank and Nicholson proposed that a more accurate approximation is to take the average of the right term at time j and at time $j+1$. They also proved that this approximation always gives stable solutions. Using the Crank and Nicholson method and deriving in a similar way to that in Section 3.2, we obtain an implicit finite difference expression of the diffusion equation (3.16)

$$A_1x_{i-1, j+1} + A_2x_{i, j+1} + A_3x_{i+1, j+1} = B_1x_{i-1, j} + B_2x_{i, j} + B_3x_{i+1, j} \quad (3.17)$$

where $A_1 = \frac{2D\Delta t}{(\Delta z_a + \Delta z_B)\Delta z_a}$,

$$A_2 = 2 \left[1 + \frac{\Delta t D}{\Delta z_a \Delta z_b} \right],$$

$$A_3 = -\frac{2D\Delta t}{(\Delta z_a + \Delta z_b)\Delta z_b},$$

$$B_1 = \frac{2D\Delta t}{(\Delta z_a + \Delta z_b)\Delta z_b},$$

$$B_2 = 2 \left[1 - \frac{\Delta t D}{\Delta z_a \Delta z_b} \right],$$

$$B_3 = \frac{2D\Delta t}{(\Delta z_a + \Delta z_b)\Delta z_b},$$

and D is the interdiffusion coefficient, Δz_a and Δz_b the adaptive mesh sizes, and Δt the time interval. For all the i 's in the z - t plane, Equation (3.17) gives an $N \times N$ matrix equation

$$\begin{bmatrix} A_1 + A_2 & A_3 & 0 & 0 & 0 & 0 \\ A_1 & A_2 & A_3 & & & 0 \\ 0 & & & & & \\ & & A_1 & A_2 & A_3 & \\ 0 & & 0 & A_1 & A_2 + A_3 & \end{bmatrix} \begin{bmatrix} x_{1,j+1} \\ x_{2,j+1} \\ \\ x_{n-1,j+1} \\ x_{n,j+1} \end{bmatrix} = \begin{bmatrix} B_1 + B_2 & B_3 & 0 & 0 & 0 & 0 \\ B_1 & B_2 & B_3 & & & 0 \\ 0 & & & & & \\ & & B_1 & B_2 & B_3 & \\ 0 & & 0 & B_1 & B_2 + B_3 & \end{bmatrix} \begin{bmatrix} x_{1,j} \\ x_{2,j} \\ \\ x_{n-1,j} \\ x_{n,j} \end{bmatrix}$$

Note that the boundary conditions have already been used in this equation. If the concentration profile at time j is known, then the concentration at time $j+1$ can be calculated from the $N \times N$ matrix equation. Thus, with the initial concentration profile, we can calculate the profile at any time. It should be noted that we could not use the Crank and Nicholson method for the Zn diffusion because the concentration dependent diffusion coefficient results in two non-linear terms in the equation.

The Zn concentration profile is determined in the previous section by solving the concentration dependent Fick's second law (3.9). The Zn concentration dependence of the Al interdiffusion coefficient is extracted from reference 66. Since the Zn concentration profile changes as the Zn diffusion proceeds, we also obtain a time-variant Al interdiffusion coefficient. In the program, we start to count the interdiffusion time when the Zn concentration in the quantum well under consideration reaches $1 \times 10^{18} \text{ cm}^{-3}$ due to the Zn diffusion since it is known that below $1 \times 10^{18} \text{ cm}^{-3}$, the interdiffusion is negligible. This saves the computing time and computer memory. The parameters used in the calculation are the same as those in the previous section. Figure 3.8 shows the calculated Al compositional profiles of the MQWs after annealing with different initial implanted Zn concentrations. The corresponding Zn profiles after the annealing are shown in Fig. 3.6 in the previous section. As shown in Figures 3.6 and 3.8, when the initial concentration C_{00} is $< 4 \times 10^{19} \text{ cm}^{-3}$, the Zn diffusion front is above the MQWs region ($x < 0.7 \text{ } \mu\text{m}$) and the MQWs are not disordered. As C_{00} is increased to $5 \times 10^{19} \text{ cm}^{-3}$, the Zn front reaches the MQWs. The Al/Ga interdiffusion occurs in the first quantum well and other quantum wells below the Zn front remain undisturbed. When C_{00} is further increased, the Zn front goes deeper into the MQWs region and the wells behind the Zinc front are gradually disordered. At $C_{00} = 2 \times 10^{20} \text{ cm}^{-3}$, the MQWs are completely disordered and become an alloy of AlGaAs with an Al composition of ≈ 0.3 , which is the average of the quantum well and barrier layers.

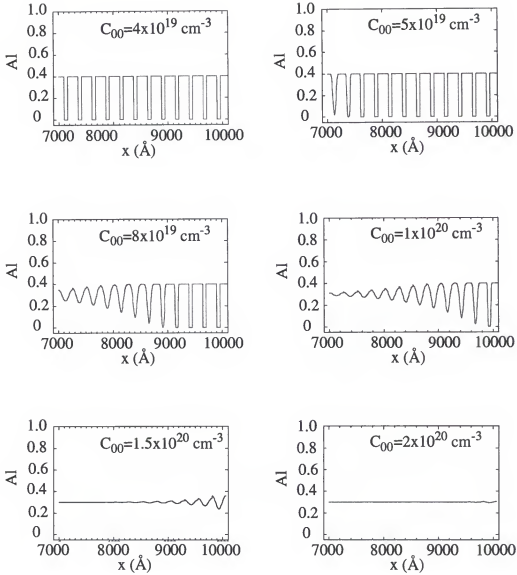


Figure 3.8 Calculated Al compositional profiles in the MQW region after annealing with various initial implanted Zn concentration C_{00}

3.4 Refractive Index Profiles of Disordered MQWs

As discussed in Section 3.1, the purpose of the MQWs disordering in the laser section is to modify the refractive index profile of the MQWs/SQW structure. It is anticipated that Al and Ga interdiffusion between the quantum well and barrier layers induced by Zn diffusion should alter the compositional profile of the quantum well structure and cause changes in band structure and energy levels, resulting in a modification of the refractive indices of the quantum wells. Compared to bulk materials, the absorption edge of a quantum well structure moves to higher energy due to quantized energy levels above the bulk band edge. The refractive index can be calculated from the absorption spectra of the quantum wells. Sophisticated band-structure techniques such as the pseudopotential method [67], the tight-binding method [68] and the hybrid band structure technique [69] have been used to calculate the real and imaginary parts of the dielectric constants of the quantum wells and superlattices. For our modeling, we use an approximation method. The refractive index of the quantum well generally includes contributions from the bulk material, the quantum effect (the absorption edge shift) and the exciton effect of the quantum well. In our MQW/SQW structure, the MQWs are designed for the modulator so that the energy of the photons emitted from the SQW laser is below the absorption edge of the MQWs. Thus, in the absorption spectra of the MQWs, the overlap between the exciton peak and the photon spectra is small leading to little contribution to the refractive index by the exciton

effect. The refractive index is mainly determined by the bulk effect when the photon energy is below the absorption edge of the quantum well. This is the base for the average index approximation for an MQW waveguide [70]. However, the average index approximation ignores the absorption edge shift to higher energy due to the quantum effect. In our model, we assume the refractive index of the GaAs/AlGaAs quantum well at optical energy below the absorption edge to be equivalent to that of the AlGaAs alloy that has the same band gap energy. This approximation has been used in the modeling of other devices in our group leading to good agreement with experimental results [42].

We first calculate the bandgap of the disordered quantum well. The quantized energy levels in the conduction and valence bands can be calculated by solving Schrodinger equation with given compositional profiles of the disordered quantum well. The equation can be written as

$$\frac{\hbar^2}{2m^*} \frac{d^2 \Psi(x)}{dx^2} + (E_n - V(x)) \Psi(x) = 0$$

where $\Psi(x)$ is the electron or hole wavefunction, $V(x)$ the band edge potential profile of the disordered quantum well determined by the compositional profile obtained in the previous section, and E_n is the energy level to be solved for. The boundary conditions for the quantum well at the interface are determined by the continuity conditions

$$\Psi_1|_i = \Psi_2|_i$$

and

$$\left. \frac{1}{m_1} \frac{d\psi_1}{dx} \right|_i = \left. \frac{1}{m_2} \frac{d\psi_2}{dx} \right|_i.$$

We use the finite difference method to solve the Schoedinger equation. Using techniques similar to those presented in Sections 3.2 and 3.3, we derive a general finite difference expression for Schroedinger equation accommodating the interface continuity conditions and the adaptive meshes. The finite difference expression for the Schoedinger equation can be written as

$$A_i \psi_{i-1} + B_i \psi_i + C_i \psi_{i+1} = 0$$

where

$$A_i = -\frac{\hbar^2}{m_{i1} \Delta x_{i1} (\Delta x_{i1} + \Delta x_{i2})}, \quad (3.18)$$

$$B_i = \frac{\hbar^2}{\Delta x_{i1} + \Delta x_{i2}} \left(\frac{1}{m_{i1} \Delta x_{i1}} + \frac{1}{m_{i2} \Delta x_{i2}} \right) + V_i - E, \quad (3.19)$$

$$C_i = -\frac{\hbar^2}{m_{i2} \Delta x_{i2} (\Delta x_{i1} + \Delta x_{i2})} \quad (3.20)$$

and V_i is the potential value at point i , E is the energy, and Δx_{i1} and Δx_{i2} the adaptive mesh sizes at point i . For all the i 's, the finite difference equation becomes an $N \times N$ matrix equation

$$\begin{bmatrix} B_1 & C_1 & & & \\ A_2 & B_2 & C_2 & & \\ & & & & \\ & & A_{n-1} & B_{n-1} & C_{n-1} \\ & & & A_n & B_n \end{bmatrix} \begin{bmatrix} \psi_1 \\ \psi_2 \\ \\ \psi_{n-1} \\ \psi_n \end{bmatrix} = 0.$$

The boundary condition that ψ_0 and ψ_{N+1} are zero, has been used. In the matrix equation, for $\psi_1, \psi_2, \dots, \psi_{n-1}$ and ψ_n to have non-trivial solution, the determinant of the $N \times N$ matrix must be zero,

$$\begin{bmatrix} B_1 & C_1 & & & \\ A_2 & B_2 & C_2 & & \\ & & & & \\ & & A_{n-1} & B_{n-1} & C_{n-1} \\ & & & A_n & B_n \end{bmatrix} = 0. \quad (3.21)$$

Note that A_i, B_i , and C_i , $i=1, 2, \dots, N$ in Equations (3.18), (3.19), and (3.20) are functions of unknown energy E . Solving Equation (3.21) for E gives a set of discrete energy values E_n which are the allowed energy levels in the quantum well.

Once the energy levels in the conduction and valence bands and hence the bandgap of the disordered quantum well are obtained, we can calculate the refractive index using Afromowitz's refractive index model for the $\text{Al}_x\text{Ga}_{1-x}\text{As}$ material [71], according to our approximation approach. In the calculation, we assume the parabolic band structure and a ratio of 0.62:0.38 is used for barriers in the conduction band and the valence band. The potential profile $V(x)$ or V_i of the disordered quantum well is obtained from the composi-

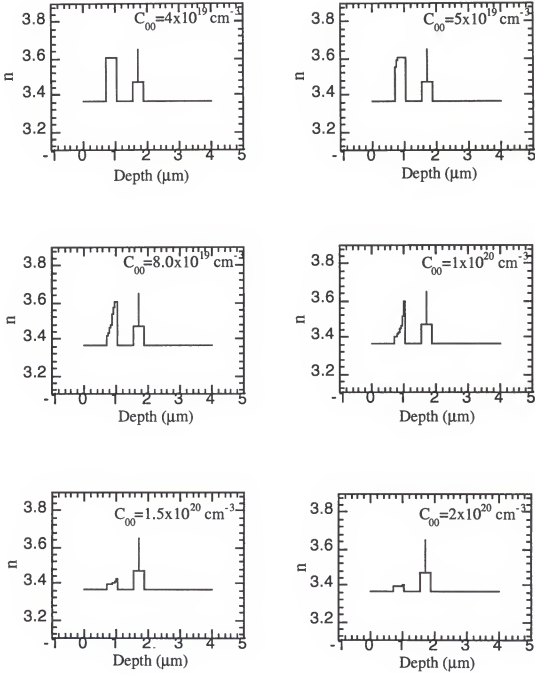


Figure 3.9 Calculated refractive index profiles of the MQW/SQW structure with the MQWs disordered under various initial Zn concentration C_{00}

tional profile calculated in the previous section. Figure 3.9 shows the calculated refractive index profiles of the MQW/SQW structure with the MQWs disordered under various initial implanted Zn concentrations. The corresponding Zn concentration profiles and the Al compositional profiles of the disordered quantum wells are shown in Figures 3.6 and 3.8. As shown in Figure 3.9, the refractive index of the MQWs are gradually modified along the depth direction as the initial implanted Zn concentration is increased and the Zn front goes deeper. When the initial concentration is increased to $\sim 2 \times 10^{20} \text{ cm}^{-3}$, the MQWs are completely disordered and its refractive index reduces to that of an $\text{Al}_x\text{Ga}_{1-x}\text{As}$ alloy with $x \approx 0.30$. This would dramatically improve the optical confinement of the lasing light in the SQW active layer.

3.5 The Optical Confinement Factor

As we discussed in Section 3.1, the threshold current density of a laser is inversely proportional to the optical confinement factor which is defined as

$$\Gamma = \frac{\int_{-\infty}^{\infty} |E|^2 da}{\int_{-\infty}^{\infty} |E|^2 da}$$

where E is the field profile of the normal mode in the SQW/MQW structure and a represents the SQW active layer. When the refractive index profile of the MQWs is modified by

the Zn induced disordering, the field profile is altered accordingly leading to a change in the optical confinement factor. We calculate the confinement factors with disordered MQWs modeled in the previous sections.

Although the MQWs and the SQW SCH in the MQW/SQW structure are two single mode waveguides, the whole structure can be considered a multilayer waveguide, as we discussed in Sections 2.1 and 2.3. The normal mode field profile of the multilayer waveguide, representing the optical field distribution in the MQW/SQW structure, can be calculated using the multilayer stack theory. Figure 3.10 shows a q -layer waveguide with the coordinates in the transverse direction of the waveguide. From the wave equation, the field profile in each layer can be expressed as

$$E_i(x) = \begin{cases} a_i \cos u_i + b_i \sin u_i & N \leq n_i \\ a_i \cosh u_i + b_i \sinh u_i & N > n_i \end{cases} \quad i = 1, 2, \dots, q \quad (3.22)$$

where

$$u_i = \kappa_i(x - x_i),$$

$$\kappa_i = \sqrt{|\beta^2 - k_0^2 n_i^2|},$$

$$N = \frac{\beta}{k_0}, \text{ the mode index,}$$

and β is the propagation constant, and n_i the refractive index in layer i . a_i and b_i are the coefficients determined by the boundary conditions. At the interface between layer i and $i+1$, the field must satisfy the boundary conditions

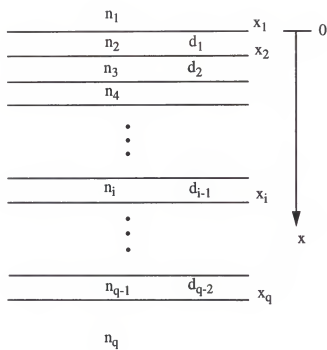


Figure 3.10 A q -layer waveguide.

$$E_i(x_i) = E_{i+1}(x_i)$$

and

$$\frac{d}{dx}E_i(x_i) = \frac{d}{dx}E_{i+1}(x_i).$$

These two boundary conditions lead to a relationship between the field amplitudes in layers i and $i+1$

$$\begin{bmatrix} a_i \\ b_i \end{bmatrix} = M_i(N) \begin{bmatrix} a_{i+1} \\ b_{i+1} \end{bmatrix} \quad (3.23)$$

where $M_i(N)$ is the characteristic matrix of the layer whose elements are functions of the mode index N . Physically, for a guided mode, the field must exponentially decay in the outer-most layers ($i=1$ and q). Since in these two layers $N > n_i$, the fields are expressed in terms of \cosh and \sinh functions in (3.22). To represent the exponentially decaying fields in these two layers, the coefficients in (3.22) should satisfy $a_1 = b_1$ and $a_q = -b_q$, so that under the coordinate system shown in Figure 3.10,

$$E_1(x) = a_1 \cosh u_1 + b_1 \sinh u_1 = a_1 e^{u_1}$$

and

$$E_q(x) = a_q \cosh u_q + b_q \sinh u_q = a_q e^{-u_q}.$$

On the hand, if we use Equation (3.22) successively from layer 1 to layer q , we can get

$$\begin{bmatrix} a_1 \\ b_1 \end{bmatrix} = M_1(N)M_2(N)\dots M_{q-1}(N) \begin{bmatrix} a_q \\ b_q \end{bmatrix} \quad (3.24)$$

If we use the decaying conditions, i.e., $a_j=b_j$ and $a_q=-b_q$, and assign an arbitrary value to a_q , say, $a_q=1$, then Equation (3.24) becomes

$$\begin{bmatrix} a_1 \\ a_1 \end{bmatrix} = M_1(N)M_2(N)\dots M_{q-1}(N) \begin{bmatrix} 1 \\ -1 \end{bmatrix}. \quad (3.25)$$

The two equations in (3.25) can then be solved for the two unknowns N and a_j . The values of N are the effective indices of the normal modes. Once N and a_j are obtained, the field profiles of the normal modes can be calculated using Equations (3.23) and (3.22). Note that we assigned an arbitrary value to a_q so the field profile is not normalized. But this does not influence the results of the confinement calculation.

Figure 3.11 shows the calculated optical field profiles in the laser section with disordered MQWs. The refractive index profiles of the disordered MQWs are obtained from the previous sections. At $C_{00} = 4 \times 10^{19} \text{ cm}^{-3}$, the MQWs are not disordered and have higher refractive indices than those of the surrounding layers, forming a guiding layer with the field of the fundamental mode well confined in it. This results in an optical confinement factor of ≈ 0 in the SQW active layer. When C_{00} increases, the MQWs are gradually disordered and the refractive index profile changes accordingly, resulting in an alteration in the field profile and the optical confinement factor in the SQW layer. At $C_{00} = 9.0 \times 10^{19}$

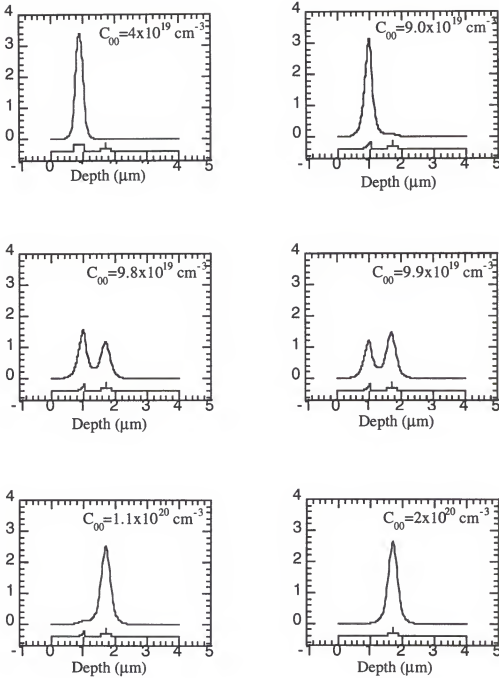


Figure 3.11 Calculated optical field profiles in the SQW/MQWs structure with the MQWs disordered under various initial Zn concentration C_{00} .

cm^{-3} , the field in the SQW waveguide starts to increase but most of the power remains in the MQW waveguide leading to a small optical confinement factor in the SQW guide. At $C_{00} = 9.8 \times 10^{19}$ and $9.9 \times 10^{19} \text{ cm}^{-3}$, the field is roughly even-split in the MQW and SQW waveguides. At $C_{00} = 1.1 \times 10^{20} \text{ cm}^{-3}$, most of the field switches over to the SQW waveguide. The quick change-over of the field distribution around $C_{00} = 9.8 \times 10^{19} \text{ cm}^{-3}$ due to the MQW disordering leads to a rapid increase in the optical confinement factor in the SQW active layer. At $C_{00} = 1.1 \times 10^{20} \text{ cm}^{-3}$, although the MQWs are not completely disordered yet, the field is well confined in the SQW waveguide and the confinement factor is close to the maximum. At $C_{00} = 2 \times 10^{20} \text{ cm}^{-3}$, the MQWs are completely disordered and become an alloy AlGaAs with an Al concentration of ≈ 0.3 whose refractive index is slightly higher than those of its cladding layers. The field profile does not change much from that for the case of $C_{00} = 1.1 \times 10^{20} \text{ cm}^{-3}$. Figure 3.12 shows the variation of the optical confinement factor with C_{00} . As we analyzed earlier, the optical confinement factor increases sharply at around $C_{00} = 9.8 \times 10^{19} \text{ cm}^{-3}$ and remains nearly constant for C_{00} equal to and greater than $1.1 \times 10^{20} \text{ cm}^{-3}$.

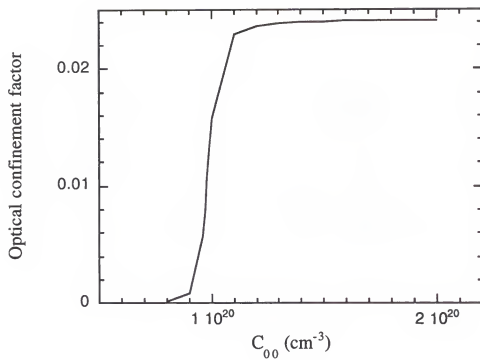


Figure 3.12 Calculated optical confinement factor vs. C_{00} .

3.6 The Lasing Threshold Current Density

We have calculated the optical confinement factor for the light in the SQW active layer of the MQW/SQW structure with different degree of the MQW disordering. In this section, we investigate the variation of the lasing threshold current density with the disordering parameters. The lasing condition can be expressed as

$$\Gamma g_{th} = \alpha_i + \frac{1}{2L} \ln \frac{1}{r_1 r_2} \quad (3.26)$$

where g_{th} is the threshold gain, Γ is the optical confinement factor, α_i is the internal loss in the laser cavity, L is the cavity length, and r_1 and r_2 are the reflectivities of the two reflection facets. The terms on the right-hand side of Equation (3.26) are basically determined by the material, its quality, and the device dimensions. With the confinement factor calculated from the previous section, we can determine the threshold gain g_{th} using Equation (3.26). Through the relation between the gain and the injected carrier density, we can obtain the threshold current density.

We first outline the gain calculation. As we discussed in Section 2.2, in a quantum well, the energy band splits into a series of subbands. The transition rate of an electron between a conduction band state and a valence band state is given by Fermi's golden rule [72] and it is proportional to the transition matrix element $|M_T|^2$ which is determined by

the band structure and the transition energy $E_{eh} = \hbar\omega$. For a given transition energy $\hbar\omega$ the density of the conduction and valence state pairs is given by a reduced density of states ρ_{red} which is determined by the density of states in the conduction band and valence band. Thus, the total transition rate W is determined by the product of the transition matrix element, the reduced density of states and the Fermi-Dirac distributions f_c and f_v in the conduction and valence bands, the latter giving the probability of a state being occupied by an electron. A downward transition from the conduction band to the valence band generates a photon while an upward transition from the valence band to the conduction band absorbs one. The optical gain g is defined as the fractional increase in photons per unit length, which is determined by the difference of the downward and upward transition rates and can be expressed as

$$g(\hbar\omega) = C|M_T|^2 \rho_{red}(f_c - f_v). \quad (3.26)$$

For detailed derivations and expressions, the readers are referred to reference 35.

To determine the Fermi levels for the Fermi-Dirac distributions, we use the relations

$$N = 2 \int_{E_c}^{\infty} \rho_c f_c dE = 2 \rho_c \sum_n \int_{E_{c_n}}^{\infty} f_c dE \quad (3.27)$$

and

$$P = 2 \int_{-\infty}^{E_v} \rho_v (1 - f_v) dE = 2 \rho_v \sum_n \int_{-\infty}^{E_{f_n}} (1 - f_v) dE \quad (3.28)$$

where N and P are injected electron and hole densities, respectively, and f_c and f_v are Fermi distributions with unknown quasi-Fermi level E_{fc} and E_{fv} . E_{fc} and E_{fv} can be numerically calculated from Equations (3.27) and (3.28) for given N and P . Note that we used the fact that for quantum wells, the density of states is constant and the energy bands are divided into subbands.

From Equation (3.26), we obtain the gain spectra for given densities of injected carriers. Because of the spectral broadening associated with each transition of energy $\hbar\omega$, a convolution of g with a Lorentzian lineshape function is performed. The calculated maximum gain g_{max} in the gain spectrum versus the injected carrier density N is plotted in Figure 3.13. The calculation is based on the 90 Å GaAs/Al_{0.2}Ga_{0.8}As single quantum well laser used in the integration. Under the steady state condition, the injected current density J and the carrier density N are related by

$$J = e L_z \frac{N}{\tau} \quad (3.29)$$

where L_z is the well thickness and the carrier lifetime $\tau=1/(BN)$. Using (3.29), the $g_{max} \sim N$ curve (Figure 3.13) is converted to the $g_{max} \sim J$ shown in Figure 3.14.

The threshold gain is determined by (3.25) with the optical confinement factor calculated from the previous sections. The corresponding threshold current density then can

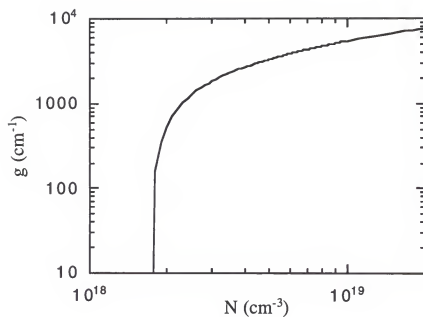


Figure 3.13 Calculated peak gain g_{\max} in the gain spectrum versus the injected carrier density N .

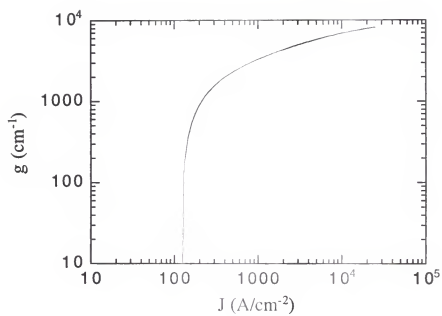


Figure 3.14 Calculated g_{\max} as a function of injected current density J

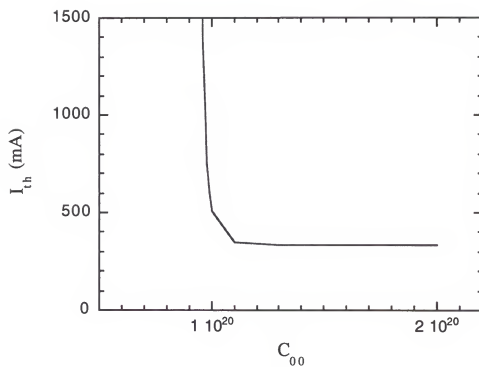


Figure 3.15 Calculated I_{th} vs. C_{00} . (50 μm x 500 μm stripe)

be obtained from the gain calculation outlined above. Figure 3.15 shows the calculated threshold current density as a function of the initial Zn concentration. The threshold current density decreases rapidly as the initial concentration of implanted Zn increases and reaches the minimum when the MQWs are completely disordered. The sharp decrease in the threshold current density corresponds to the sharp increase in the optical confinement factor, which is the result of the refractive index decrease of the cladding layer by the MQW disordering.

In this chapter, we modeled the Zn diffusion induced disordering in the MQW/SQW structure and investigated the variation of the threshold current density of the SQW laser with the MQW disordering. We predicted a rapid reduction in the lasing threshold when the MQW cladding layer of the SQW laser is totally disordered. The results of the numerical simulation will be compared with the experimental results in Chapter 5.

CHAPTER 4

GROOVE BETWEEN THE LASER AND THE TAPER

The Zn disordered MQW region discussed in Chapter 3 acts as the p contact cladding layer for the laser section. However we still need to provide a mechanism for forming the laser cavity as well as a means of coupling the laser output to the tapered waveguide section. The groove, etched between the laser section and the tapered coupler (Figure 2.7), plays a key role in this connection. It functions as a partially transmissive mirror. The reflection from the groove provides the necessary feedback for the lasing action and the transmission couples light from the laser to the tapered coupler. In this chapter, we investigate the reflectance from the groove and its influence on the lasing threshold and power output.

4.1 The Characteristic Matrix

In this section, we first discuss the reflection and transmission from a three layer structure using a matrix method [73] and then apply the matrix method to the reflection problem for the groove in the next section.

The three layer structure, with a layer of thickness d and refractive index n_1 , sandwiched between two infinite thick layers of refractive indices n_0 and n_2 , is shown in Figure

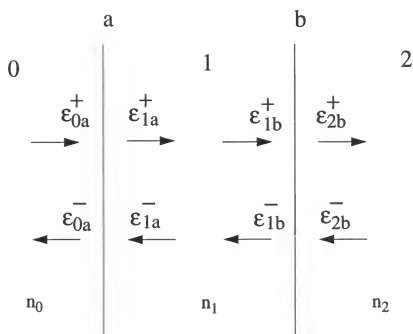


Figure 4.1 Reflection and transmission from a three layer structure.

4.1. The electric field incident at bulk interfaces a and b between the three layers is reflected from and transmitted through the interfaces. The field in each region can be expressed as two waves: forward traveling and backward traveling, as shown in Figure 4.1. If light is launched into the three-layer structure from region 0, the forward traveling wave represents the transmitted light while the backward traveling wave represents the reflected light. The notation used to designate the waves is as follows. The number in the subscript represents the region where the wave travels, the letter represents the interface on which the wave is incident, and the + and - signs represent forward and backward traveling waves, respectively. The total electric fields at the interface a in region 0 and 1 thus can be expressed as

$$\epsilon_{0a} = \epsilon_{0a}^{+} + \epsilon_{0a}^{-}$$

and

$$\epsilon_{1a} = \epsilon_{1a}^{+} + \epsilon_{1a}^{-}.$$

For normal incident, the field is continuous at the interface, $\epsilon_{0a} = \epsilon_{1a}$, thus

$$\epsilon_{0a}^{+} + \epsilon_{0a}^{-} = \epsilon_{1a}^{+} + \epsilon_{1a}^{-}. \quad (4.1)$$

For magnetic fields at the interface, similar relations hold and we have

$$y_0(\epsilon_{0a}^{+} - \epsilon_{0a}^{-}) = y_1(\epsilon_{1a}^{+} + \epsilon_{1a}^{-}). \quad (4.2)$$

where y_0 and y_1 are the wave admittance in regions 1 and 2, respectively. From Equations (4.1) and (4.2), we can express the forward and backward traveling waves in the region 0

in terms of those in region 1 in a matrix form,

$$\begin{bmatrix} \varepsilon_{0a}^+ \\ \varepsilon_{0a}^- \end{bmatrix} = \frac{1}{t_a} \begin{bmatrix} 1 & r_a \\ r_a & 1 \end{bmatrix} \begin{bmatrix} \varepsilon_{1a}^+ \\ \varepsilon_{1a}^- \end{bmatrix} \quad (4.3)$$

where

$$r_a = \frac{n_0 - n_1}{n_0 + n_1}$$

and

$$t_a = \frac{2n_0}{n_0 + n_1}.$$

When the forward and backward waves travel between the two interfaces a and b , the accumulated phases and the fields at the two interfaces are related by

$$\varepsilon_{1a}^+ = \varepsilon_{1b}^+ e^{-j\delta_1}$$

and

$$\varepsilon_{1a}^- = \varepsilon_{1b}^- e^{j\delta_1}.$$

where $\delta_1 = k_0 n_1 d$ is the phase change. They can be expressed in a matrix form

$$\begin{bmatrix} \varepsilon_{1a}^+ \\ \varepsilon_{1a}^- \end{bmatrix} = \begin{bmatrix} e^{-j\delta_1} & 0 \\ 0 & e^{j\delta_1} \end{bmatrix} \begin{bmatrix} \varepsilon_{1b}^+ \\ \varepsilon_{1b}^- \end{bmatrix}. \quad (4.4)$$

Using Equations (4.3) and (4.4), we can relate the fields in the regions 0 and 2,

$$\begin{bmatrix} \epsilon_{0a}^+ \\ \epsilon_{0a}^- \end{bmatrix} = \frac{1}{t_a} \begin{bmatrix} 1 & r_a \\ r_a & 1 \end{bmatrix} \begin{bmatrix} e^{-i\delta_1} & 0 \\ 0 & e^{-i\delta_1} \end{bmatrix} \frac{1}{t_b} \begin{bmatrix} 1 & r_b \\ r_b & 1 \end{bmatrix} \begin{bmatrix} \epsilon_{2b}^+ \\ \epsilon_{2b}^- \end{bmatrix}$$

Therefore, the reflectance R and transmittance T for the three layer structure can be calculated from this equation. We call the matrices in Equations (4.3) and (4.4) the characteristic matrices. By successively using the characteristic matrices, we can obtain the reflectance and transmittance of a multilayer structure.

4.2 Reflectance from the Groove

In semiconductor lasers, usually two cleaved facets are used as reflectors to form a laser cavity. The reflectance from the facets is determined by the crystal material. For GaAs/AlGaAs lasers, the reflectance of the cleaved facets is about 0.3.

In our integrated structure, a groove etched between the laser section and the tapered coupler functions as a reflector while the other reflector is formed by a cleaved facet. The groove, together with the laser and the tapered coupler, forms a multilayer structure shown in Figure 4.2. We can calculate the reflectance of the groove using the matrix method discussed in the previous section. Note that the refractive index in the tapered waveguide coupler is not constant along the taper because of the tapering. We calculated the mode index profile of the fundamental mode along the taper using the Multilayer stack theory discussed in Section 3.5. The index profile along the taper is shown in

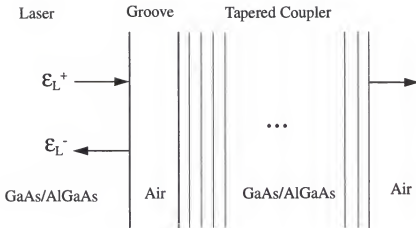


Figure 4.2 The multilayer model for the reflectance calculation. The taper section is approximated by a series of small steps.

Figure 4.3. The tapered waveguide coupler is designed so that the evolution of the field propagating along the taper remains adiabatic and the light launch into the taper as the fundamental mode remains in the fundamental mode as it propagates along the tapered coupler.

The reflectance due to the groove is defined as

$$R = \left| \frac{\mathcal{E}_L^+}{\mathcal{E}_L^-} \right|^2$$

where \mathcal{E}_L^+ is the forward traveling wave incident on the groove and \mathcal{E}_L^- is the backward traveling wave reflected from the groove, as shown in Figure 4.2. In the calculation outlined in the last section, using the multilayer matrix method, the mode index of the fundamental mode in the MQW/SQW structure with MQWs completely disordered is used as the refractive index of the laser section (layer 0 in Figure 4.2). The tapered waveguide coupler is divided into many small sections along the taper direction so that the mode index profile in Figure 4.3 is approximated by a series of small steps. The reflectance of the groove is calculated by repetitively using the characteristic matrices defined in the last section. The calculated reflectance versus the groove width is shown in Figure 4.4. The reflectance oscillates with respect to the groove width since the groove forms a Fabry-Perot cavity. It should be noted in the figure that the reflectance of the groove can be significantly higher than that of a cleaved facet (~ 0.3). This should reduce the lasing threshold.

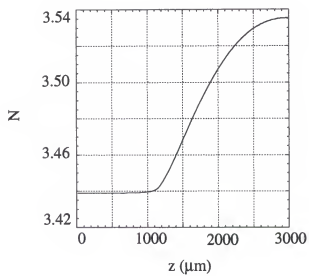


Figure 4.3 The mode indices along the tapered waveguide

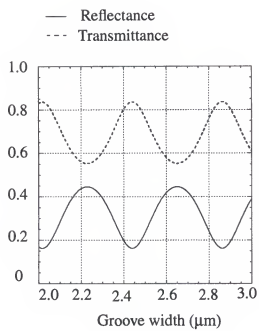


Figure 4.4 Calculated reflectance of the groove versus the groove width.

4.3 The Lasing Threshold Variation

The relationship between the lasing threshold and the reflectance of the reflectors can be expressed as

$$\Gamma g_{th} = \alpha_i + \frac{1}{2L} \ln \frac{1}{r_1 r_2} \quad (4.5)$$

where g_{th} is the threshold gain, Γ the optical confinement factor, α_i the internal loss, L the cavity length, and r_1 and r_2 the reflectance of the two facets. This relation shows higher reflectance results in lower lasing threshold as more light is reflected so that the cavity experiences less external loss.

To analyze the variation of the threshold current density with the groove width, we use a simple approach, instead of the rigorous analysis in Chapter 3. Generally, the threshold current density J_{th} is proportional to the threshold gain g_{th} , $J_{th} = \beta g_{th}$. From Equation (4.5), we then have

$$J_{th} = \frac{1}{\Gamma \beta} \left(\alpha_i + \frac{1}{2L} \ln \frac{1}{r_1 r_2} \right).$$

The threshold current densities of the two lasers from the same wafer, one with an etched groove (J_{th}^g) and the other with two cleaved facets (J_{th}^c) can be related as

$$\frac{J_{th}^g}{J_{th}^c} = \frac{\alpha + \frac{1}{2L} \ln \frac{1}{r_0 r_g}}{\alpha + \frac{1}{L} \ln \frac{1}{r_0}} \quad (4.6)$$

where r_0 and r_g are reflectivities of the cleaved facet and the groove, respectively. With an assumed J_{th}^c we can calculate the variation of J_{th}^g with the groove width d from Equation (4.6) since the r_g vs. d relation is known from the calculation in the previous section. We assume $I_{th}^c = 400$ mA. The calculated threshold current of the laser as a function of the groove width is shown in Figure 4.5.

4.4 Power Output Variation

In this section, we investigate how the groove width affects the ratio between the power output from the taper side (P_T) and from the laser side (P_L) (Figure 4.6). On the laser side, the reflection is provided by a cleaved facet with a reflectance R_L and transmittance T_L . On the taper side, the feedback for the laser is provided by the composite groove-taper structure (Figure 4.2) which is represented by equivalent reflectance R_T and transmittance T_T (Figure 4.6) calculated in Section 4.2. The forward and backward traveling waves in each region are also shown in Figure 4.6. The power output from each side can thus be expressed as

$$P_T = \int \frac{|E_{2T}^+|^2}{\eta} da$$

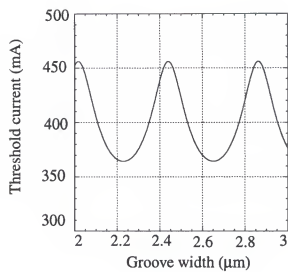


Figure 4.5 Calculated threshold current versus the groove width.

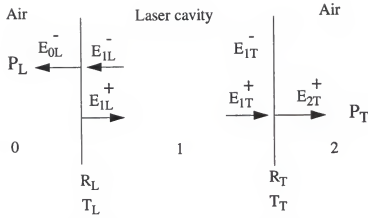


Figure 4.6 Fields and output power in the laser cavity.

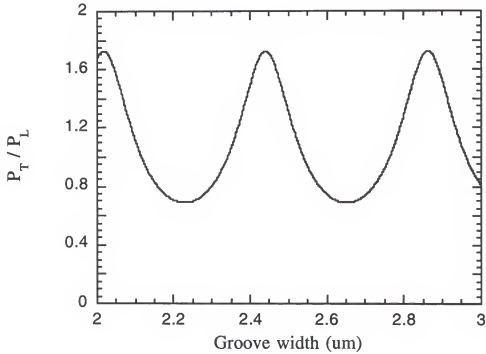


Figure 4.7 Calculated ratio of power output from the taper side P_T and from the laser side P_L vs. the groove width.

and

$$P_L = \int \frac{|E_{0L}|^2}{\eta} da$$

In the laser cavity with net gain, $g\text{-}\alpha$, the fields at the two facets are related by a factor $e^{(g\text{-}\alpha)L}$ or $e^{-(g\text{-}\alpha)L}$ depending on the direction of wave propagation. With the lasing condition

$$R_L R_T e^{(g\text{-}\alpha)L} = 1,$$

the ratio between the power output from the two sides is found to be

$$\frac{P_T}{P_L} = \frac{T_T \sqrt{R_L}}{T_L \sqrt{R_T}}.$$

Since R_T and T_T are functions of the groove width, the power ratio varies with the groove width. Figure 4.7 shows the calculated power ratio as a function of the groove width. The ratio varies between 0.7 and 1.7.

In this chapter, we have investigated the dependence of the reflectance from the groove and the corresponding lasing threshold current on the groove width. As expected, both the reflectance and the threshold current oscillate with the groove width. Potentially, their performance can be significantly improved over their counterparts viz., the cleaved facet lasers.

CHAPTER 5

FABRICATION TECHNIQUES AND EXPERIMENTAL RESULTS

In this chapter, following the discussion on material growth, we investigate the key fabrication techniques and the associated experimental results including the MQW disordering by Zn implantation and annealing, the groove etching by reactive ion etching, and the fabrication of the tapered waveguide coupler. We conclude the chapter with the experimental results on the integration of the SQW laser and the tapered waveguide coupler.

5.1 Material Growth

All epitaxial growths for our samples are performed by metalorganic chemical vapor deposition (MOCVD), also known as metalorganic vapor phase epitaxy (MOVPE). Tri-Methyl Aluminum (TMA), Tri-Methyl Gallium (TMG), and Arsine (AsH_3) are used as the precursors. The metalorganic sources, TMA and TMG, are liquid at room temperature. Hydrogen carrier gas is bubbled to vaporize them and the vapor is then led to the reaction tube. AsH_3 is gas at room temperature and its flow to the reactor is controlled by valves. The gases are pyrolyzed on the hot surface of the substrate, generally at 500 - 800 °C heated by RF induction. The pyrolysis reaction is non-reciprocal. The crystal grows contin-

uously only on the hot susceptor. The growth at other places is suppressed by the water cooled tubes. Since the gas flow rates in the reactor can be easily controlled, the compositions of the alloys and doping levels can be changed quickly leading to narrow transient regions and abrupt hetero-interfaces. MOCVD, as well as MBE, makes the growth of quantum well and superlattices structure possible.

The substrate is cleaned and etched before growth. The procedure is as follows,

- 1) Dip in boiling Trichloroethane (TCE) for 5 minutes,
- 2) dip in boiling Acetone for 5 minutes,
- 3) dip in warm methanol for 2 minutes,
- 4) rinse in DI water,
- 5) etch in the $\text{NH}_4\text{OH}:\text{H}_2\text{O}_2:\text{H}_2\text{O}$ solution with ratio of 20:7:100 for 5 minutes
to remove possible damage on the wafer surface caused by lapping and polishing
of the wafer,
- 6) rinse in DI water and
- 7) blow dry by N_2 .

We use an atmospheric pressure horizontal reactor. The growth is at a temperature of 725 °C. The growth rate used is 300 Å/minute with a V/III mole ratio of 40. n-type doped GaAs wafers of (100) orientation are used as substrates. Figure 5.1 shows the P-I curve of a SQW laser (without the MQWs) we grew. In addition to the samples we grew here at UF, we also used the samples from outside vendors.

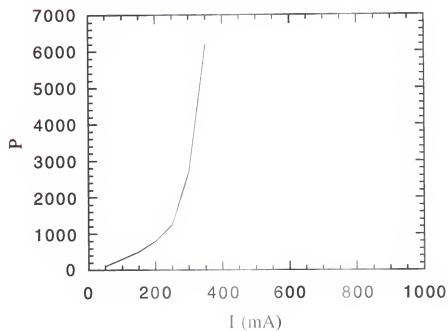


Figure 5.1 P-I curve of a regular SQW laser ($100\text{ }\mu\text{m} \times 500\text{ }\mu\text{m}$).

5.2 MQW Disordering by Zn Implantation and Annealing

In Chapter 3, we modeled the Zn induced disordering of the MQWs. Zn is first introduced into the sample by ion implantation and the subsequent annealing disorders the MQWs. Ion implantation is the introduction of energetic charged particles into targets with sufficient energy to penetrate beyond the surface region. A beam of dopant ions with fixed energy is rastered across the sample surface. The penetration depth is determined by the energy of the incident ions. They enter the crystal lattice, collide with the atoms in the lattice, and gradually lose their energy coming to rest at some depth in the crystal. The dose of the implanted ions is determined by the ion flux and the implantation time. The flux of the charged ions forms a current that can be directly measured. Thus, the dose of the implantation can be easily controlled. Also, high concentration doping can be achieved with implantation. For these reasons, we choose implantation over other methods such as diffusion from vapor or deposited Zn.

The Zn implantations in samples with the MQW/SQW structure (Figure 3.3) have been performed with various dose levels. The implantation energy has been kept at 165 keV which is the highest energy attainable from the implanter we used. After the Zn implantation, the sample is capped by 500 Å thick SiO₂ deposited by e-beam evaporation. The sample is then placed top-side down on a silicon wafer and annealed in a furnace at

700 °C for 40 minutes. The SiO₂ cap is used to prevent the loss of arsenic from the sample surface during the annealing.

The SQW laser with the MQW cladding layer is then fabricated from the Zn implanted and annealed sample. The procedure is as follows.

- 1) Remove the SiO₂ cap layer by Buffered Oxide Etchant (BOE) 6:1, etching for 10 seconds, then rinse in DI water and blow dry with N₂.
- 2) Spin photoresist S1400-33 at 5000 RPM for 40 sec. Bake at 90 °C for 30 min.
The thickness of the photoresist is about 1.5 µm.
- 3) Expose on the mask aligner for 7 sec. The mask pattern is 50 µm wide stripes for laser electrodes.
- 4) Develop in MF-319 for 40 sec. Rinse in DI water and Blow dry with N₂.
- 5) E-beam evaporation of Ti (200 Å) and Au (1000 Å).
- 6) Lift-off in acetone to get 50 µm wide Ti/Au electrodes.
- 7) Lap the backside until sample is ~100 µm thick.
- 8) Clean the sample in warm TCE, acetone and methanol. Rinse in DI water. Blow dry.
- 9) E-beam evaporate of AuGe for 1000 Å on the backside.
- 10) Cleave the sample into 500 µm laser bars for test.

We used various dosage of Zn implantation. At low doses (below 10¹⁵ cm⁻²) no lasing was observed. When the dose increased to the order of 10¹⁵, the device lased with

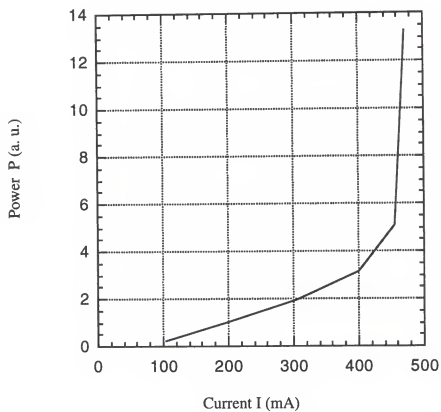


Figure 5.2 P-I curve of a MQW/SQW laser with a implant dosage of $7 \times 10^{15} \text{ cm}^{-2}$.

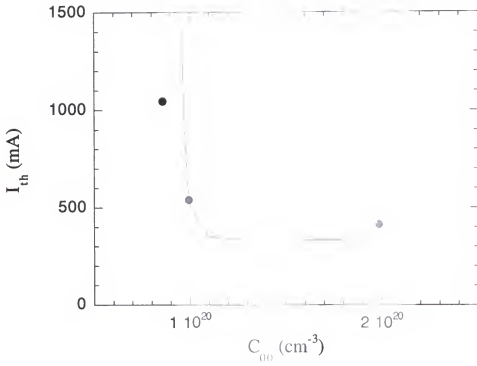


Figure 5.3 I_{th} vs. C_{00} for the SQW laser ($50 \mu\text{m} \times 500 \mu\text{m}$) with the disordered MQW cladding. The dots: experimental. The solid line: calculated.

high threshold current indicating partial disordering of the MQWs. When the dose was increased from $3 \times 10^{15} \text{ cm}^{-2}$ to $7 \times 10^{15} \text{ cm}^{-2}$, which correspond to initial concentration C_{00} of implanted Zn of 8×10^{19} to $2 \times 10^{20} \text{ cm}^{-3}$, the threshold current decreased rapidly from $\sim 1000 \text{ mA}$ to $\sim 400 \text{ mA}$. Figure 5.2 shows the P-I curve of the laser with a Zn implantation dose of $7 \times 10^{15} \text{ cm}^{-2}$. The threshold current vs. the dose is shown in Figure 5.3. The dots are experimental data and the solid line is the dependence calculated with the same disordering parameters in Chapter 3. They agree well verifying our prediction that disordering of the MQWs by Zn greatly reduces the threshold current of the SQW laser.

5.3 Groove Etching By RIE

In etching the groove with reactive ion etching (RIE), the availability of a high quality mask is important. In a conventional photoresist mask, a relatively thick layer of photoresist is needed and the edges of the patterns are generally rounded due to the anisotropic development of the photoresist in the photolithographic process. Masks with rounded edges will degrade easily during the RIE and lead to rounded groove walls. We use a tri-level mask (Figure 5.4) in which two layers of photoresist are used with a thin layer of Ti sandwiched between them. A pattern window in the top photoresist layer is opened by a photolithographic process and then the thin Ti layer in the window is etched with Cl_2 -RIE. With the remaining Ti layer serving as the mask, the bottom layer of the

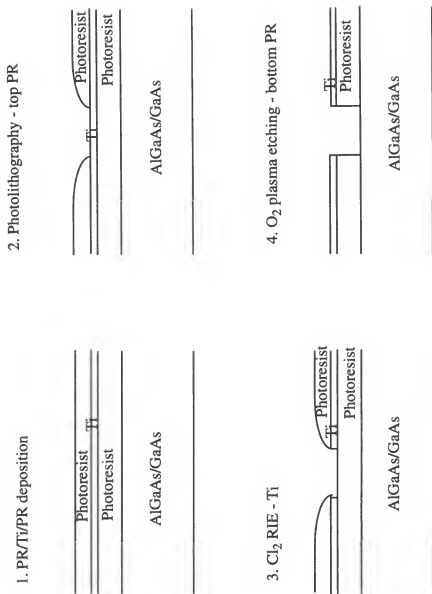


Figure 5.4 Preparation of the tri-level mask.

photoresist is etched by O_2 plasma etching. A nearly vertical wall can be obtained with a thick layer of photoresist. Another advantage of the tri-level mask is that the bottom layer of photoresist can be baked at higher temperatures to have higher resistance to RIE. To etch the GaAs/AlGaAs system, it is necessary to have high base vacuum to prevent the AlGaAs from being oxidized during RIE.

To test the etched groove, we used a conventional SQW laser structure as shown in Figures 5.5 and 5.6 (Note the absence of the MQWs). We have fabricated several lasers with an etched mirror and an etched groove, respectively. Figure 5.5 shows the measured P-I curve for a laser with an etched facet and a cleaved facet. We estimated the reflectance of the etched facet by comparing the threshold current densities of the etched-mirror laser and a control laser using Relation (4.6). The control device had the same material compositions and layer thicknesses but had two cleaved facets. We used $\alpha=8\text{ cm}^{-1}$ and $R_0=0.3$. The reflectance R_c of the etched facet was estimated to be about 0.13. The measured P-I curve for a laser with an etched groove is shown in Figure 5.6.

5.4 Fabrication of the Tapered Coupler

In this section, we present the fabrication process for the tapered waveguide coupler. The gradual disordering of the multiple quantum wells in the tapered coupler section is realized by implantation of nitrogen through a tapered SiO_2 mask and subsequent

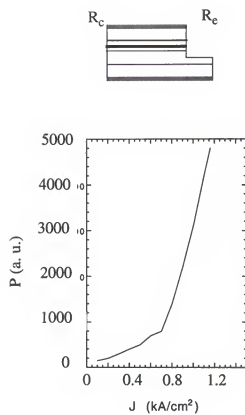


Figure 5.5 Measured P-I curve for a conventional SQW laser with an RIE etched facet.

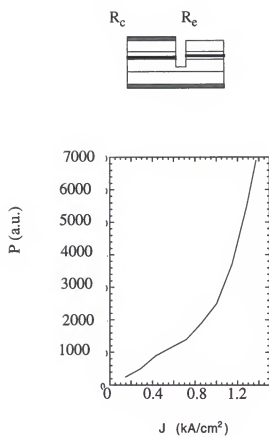


Figure 5.6 Measured P-I curve for a SQW laser with an RIE etched groove.

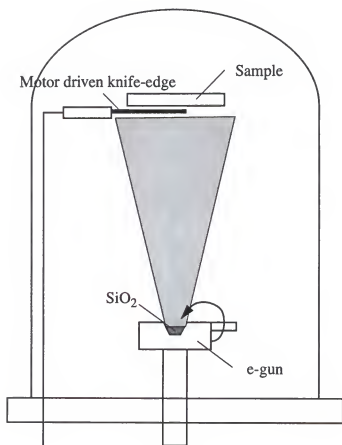


Figure 5.7 Illustration of e-beam evaporation of the tapered SiO_2 mask.

annealing. The e-beam evaporation of the tapered SiO_2 mask is illustrated in Figure 5.7. A motor driven knife-edge mask covers the sample before the evaporation starts. As the evaporation proceeds, the knife-edge moves in the direction of the tapered waveguide coupler leaving a linearly tapered SiO_2 layer on the sample. The length and thickness of the SiO_2 is controlled by adjusting the knife-edge speed and the evaporation rate of SiO_2 . In our experiments, the knife edge speed is $20 \mu\text{m}/\text{sec}$ and the evaporation rate used is $16 \text{ \AA}/\text{sec}$. For a 3 mm long coupler, we have a 0-2500 \AA thick SiO_2 taper. The sample with the tapered SiO_2 mask is implanted with Nitrogen at an implantation energy of 125 keV with a dosage of $5 \times 10^{15} \text{ cm}^{-2}$ and then annealed at 700°C for 40 minutes. Figure 5.8 shows the photoluminescence spectra of the sample along the taper. The photoluminescence peak due to the MQWs shifts along the taper indicating the MQWs are gradually disordered along the taper. Various impurities, including Zinc, Fluorine, Oxygen, and Nitrogen, have been used to disorder the MQWs in the tapered coupler section in our experiments. Nitrogen was found to provide the lowest optical loss. Losses due to the nitrogen doping was estimated by measuring the losses of a nitrogen implanted and annealed MQW waveguide without the SiO_2 cap. The measured loss was $\sim 6 \text{ dB}/\text{cm}$. In the tapered coupler, the losses due to nitrogen varied along the taper from the maximum ($\sim 6 \text{ dB}/\text{cm}$) to the minimum ($\sim 0 \text{ dB}/\text{cm}$). The average was $\sim 3 \text{ dB}/\text{cm}$. This is significantly lower than the $12 \text{ dB}/\text{cm}$ losses our group previously obtained for the Zn disordered tapered interconnect. Figure 5.9 shows the measured optical loss due to nitrogen doping.

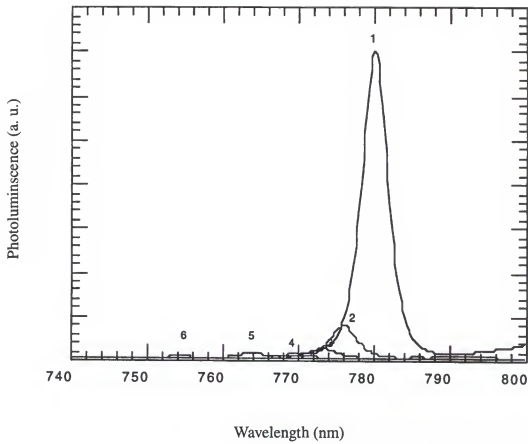


Figure 5.8 Measured photoluminescence spectra of the sample along the taper. The numbers represent different positions along the taper.

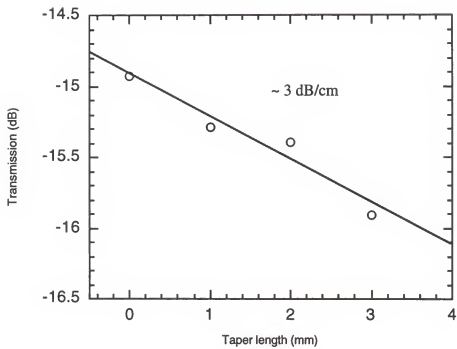


Figure 5.9 Measured optical loss of the tapered coupler.

5.5 The Integration

The fabrication process of the integration of a SQW laser and a tapered waveguide coupler (Figure 2.7) involves the material growth, the MQW disordering in the laser section, taper coupler fabrication, the etching of the groove, and the laser fabrication. The process is summarized below.

1. Material growth by MOCVD. The layer composition and thickness sequences are shown in Figure 3.3.
2. Zn implantation.
 - 1) Clean the sample in TCE, acetone, methanol and DI water
 - 2) Use copper tape as mask to cover the taper section to prevent unwanted Zn implantation in that section.
 - 3) Implant Zn at an energy of 165 keV with a dosage of $7 \times 10^{15} \text{ cm}^{-2}$.
 - 4) Clean the sample. If necessary, use the oxide plasma etch to remove any residue from the tape.
3. SiO₂ tapered mask

E-beam evaporate SiO₂ using the motor drive knife-edge. The SiO₂ evaporation rate and the knife-edge speed are 16 Å/s and 20 µm/s, respectively. The taper thickness varies from 0 to 2500 Å.

4. Nitrogen implantation

- 1) Cover the laser section with copper tape.
- 2) Implant Nitrogen at energy of $5 \times 10^{15} \text{ cm}^{-2}$.
- 3) Clean the sample. Use oxygen plasma if necessary.

5. Annealing

- 1) E-beam evaporate 500 Å thick SiO_2 on the sample
- 2) Place the sample upside down on a silicon wafer and anneal at 700 °C for 40 minutes.
- 3) Remove the SiO_2 cap layer in buffered oxide etchant (BOE)

6. Groove etching

- 1) Spin photoresist S1400-33 at 5000 RPM for 40 sec. Bake at 120 °C for 30 minutes.
- 2) E-beam evaporate 300 Å Ti.
- 3) Spin photoresist S1400-17 at 5000 RPM for 40 sec. Bake at 90 °C for 30 minutes.
- 4) Expose the groove patterns for 2.5 sec.
- 5) Develop in MIF 319 for 40 sec. Rinse in DI water and blow dry with N_2 .
Hard bake at 120 °C for 30 min.
- 6) Cl_2 reactive ion etching for Ti.
- 7) Oxygen plasma etch for the lower layer photoresist.

8) Etch the groove on the GaAs/AlGaAs substrate by Cl_2 RIE. Pump the system down to 2×10^{-7} torr before starting etching to prevent Al from being oxidized.

9) Remove the remaining photoresist.

7. Metallization for the laser

1) Spin photoresist S1400-23 at 5000 RPM for 40 sec. Bake at 90 °C for 30 minutes.

2) Expose the 50 μm stripe patterns for 4 sec.

3) Develop in MIF 319 developer for 40 sec, rinse in DI water and blow dry.

4) E-beam evaporate Ti (200 Å) and Au (1000 Å).

5) Lift-off in acetone.

6) Lap the backside until the sample thickness is $\sim 100 \mu\text{m}$.

7) Clean the sample in warm TCE, acetone and methanol, rinse in DI water and blow dry.

8) E-beam evaporate 1000 Å thick AuGe on the backside of the sample.

9) Cleave the sample for measurements.

Utilizing the techniques we have developed, the integration of a GaAs/AlGaAs SQW laser and a tapered waveguide coupler has been accomplished. Figure 5.10 shows the I-V curve of the laser diode of the integrated structure. The P-I curve of the laser is shown in Figure 5.11. We also compared the power output from the laser side and from the

taper side at various injection current levels. The output from the taper side is about 5% of that from the laser side, which is much lower than that in the ideal case we calculated in Section 4.4. Scattering due to the roughness of the etched groove facets and diffraction in the groove may have caused much of the losses. Further work is necessary to reduce the roughness of the etched groove and hence increase the output. Another possibility would be to incorporate a DFB structure for the laser section. Unfortunately, it comes at the expense of material regrowth.

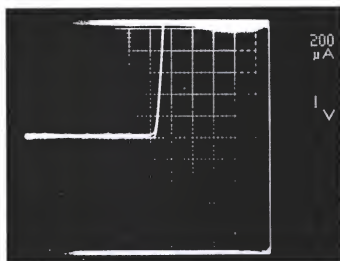


Figure 5.10 Measured I-V curve of the laser diode in the integrated structure.

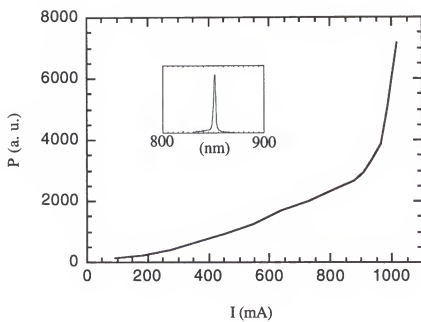


Figure 5.11 Measured P-I curve of the laser in the integrated structure.

CHAPTER 6

SUMMARY AND CONCLUSIONS

In this dissertation, we studied theoretically and experimentally a novel monolithic integration of a single quantum well laser and a tapered waveguide coupler in the GaAs/AlGaAs materials. Compared to the existing laser-waveguide integration structures using butt coupling or directional coupling, this integration scheme avoids complicated and costly material regrowth without sacrificing the design and fabrication flexibilities.

The key technologies in this integration are the disordering of the multiple quantum wells (MQW) in both the laser section and the tapered coupler section, and etching of a groove between the laser section and the tapered coupler section. The single quantum well (SQW) waveguide for the laser and the MQW as the output waveguide for modulation are vertically stacked. The disordering of the MQWs in the laser section is necessary in order to achieve low threshold current density for the laser. We numerically modeled Zn induced disordering of the MQWs. We first used an explicit finite difference method to solve the diffusion equation in which the diffusion coefficient is concentration dependent. The resulting numerical Zn diffusion profile as a function of time is used to calculate the (Zn) concentration dependent interdiffusion coefficient of Al and Ga in the quantum well and barrier layers. Although some researchers have used the Boltzmann–Matano method

and the error function approximation to investigate the Zn induced interdiffusion, they ignored the time dependence of the interdiffusion coefficient and the two methods are not applicable to the problem we are dealing with. We developed a finite difference approach for solving the interdiffusion profile. An implicit method was used to ensure the solution stability. The Zn diffusion in the MQWs alters the compositional profile of the MQWs resulting in a modification of the refractive index profile. We continued the process to calculate this modified refractive index profile. We assumed the refractive index of the quantum well is equivalent to that of the AlGaAs alloy that has an identical bandgap since the exciton effect contribution to the refractive index is negligible when the optical energy is far below the bandgap. We again used the finite difference method to solve the Schrodinger equation for the energy levels in the disordered quantum well and then calculated the corresponding refractive index profile in the MQW/SQW laser structure. The disordering of the MQWs influences the laser performance through the optical confinement in the SQW active layer. With the modified refractive index profile, we calculated the variation of the optical confinement factor with the disordering parameter using the multilayer stack matrix theory. Finally, we performed the gain calculations for the SQW laser and investigated the dependence of the threshold current density on the disordering of the MQWs. We predicted a sharp reduction in the threshold current density when the MQWs are disordered, which agreed well with our experimental results obtained later.

The etched groove between the laser section and the taper coupler functions as a partially transmissive mirror providing the needed feedback for the laser. The reflectance

of the groove was investigated by using a multilayer matrix method. The laser, groove, and tapered coupler were considered as “layers” in the light propagation direction, with the taper being further divided into many “layers” so the taper can be approximated by a series of small steps. The mode index of the fundamental normal mode is used as the refractive index in each layer. The reflectance of the groove was thus calculated as a function of the groove width. We found the reflectance oscillates with respect to the groove width and its value can be significantly larger than that of a cleaved facet. We used a simple approach to calculate the threshold current of the laser with an etched groove, in which the threshold current of the etched groove laser is expressed in terms of known parameters of a laser from the same wafer but with two cleaved facets. The threshold current can be reduced with appropriate groove widths. However, the dependence of the threshold current on the groove width was rather difficult to measure due to the nonuniformity of the etched groove and the scattering associated with it. As such, no correlation could be established.

We developed key fabrication techniques for the integration. Zn induced disordering was realized by Zn implantation and subsequent annealing. Implantation was chosen over vapor or film (deposited) diffusion because of its ease in controlling of the dose in as wide a range as possible. We used various implantation dosage and successfully reduced the threshold current from over 1000 mA to ~400 mA by increasing the implantation dosage indicating the disordering of the MQWs occurring as predicted by our numerical simulation. The groove between the laser section and the taper was etched by Cl_2 reactive etching (RIE). We used a tri-level mask to improve the mask quality and ensure vertical

walls in the groove. Regular SQW lasers with etched facet and etched groove were successfully fabricated but showed nearly twice high threshold current as the lasers with two cleaved facets, presumably because of the roughness of the etched facets. Using these techniques, we have successfully fabricated a laser-taper coupler integrated device although the threshold current and the loss are somewhat higher.

In conclusion, we have investigated theoretically and experimentally the key techniques for the integration including the Zn induced disordering of the MQWs in the laser section and the etched groove, and demonstrated the integration of a SQW laser and tapered coupler in the GaAs/AlGaAs material system without any regrowth. Coupled with other research efforts in the Photonics Research Laboratory on the tapered waveguide coupler as well as in electroabsorption modulator, this dissertation, in effect, completes the integration of the SQW laser - MQW absorption modulator via a tapered waveguide coupler in GaAs/AlGaAs without any regrowth. Further research is necessary in order to optimize the groove etching process as well as improve the device performance.

REFERENCES

- [1] M. S. Goodman, H. Kobrinski, M. P. Vecchi, R. M. Bulley, and J. L. Gimlett, The LAMBDANET Multiwavelength Network: Architecture, Applications and Demonstrations, *IEEE J. Selected Areas Commun.* 8(6), 995-1004 (1990).
- [2] K. Oda, M. Fukutoku, and H. Toba, 128 channel, 480km FSK-DD transmission experiment using 0.98 mm pumped erbium-doped fiber amplifiers and a tunable gain equalizer, *Electron. Lett.*, 30(12), 982-984, (1994).
- [3] N. Chinone, Spectral change in semiconductor lasers due to pulsation. *Nat. Conv. Rec. of IECE Japan*, no.885, (1973).
- [4] K. Stubkjaer, M. Asada, S. Arai, and Y. Suematsu, Spontaneous recombination, gain, and refractive index variation for 1.6 μm wavelength InGaAsP/InP lasers, *Jpn. J. Appl. Phys.*, 20(8), 1499-1505, (1981).
- [5] M. Ito and T. Kimura, Carrier density dependence of refractive index in AlGaAs semiconductor lasers, *IEEE J. Quantum Electron.*, QE-16, 910-911, (1980)
- [6] J. S. Manning and Olshansky, Carrier induced index change in AlGaAs double-heterostructure lasers, *Electron. Lett.*, 17, 506-507, (1981).
- [7] K. Kishino, S. Aoki, and Y. Suematsu, Wavelength variation of 1.6 μm wavelength buried heterostructure GaInAsP/InP lasers due to direct modulation. *IEEE J. Quantum Electron.*, QE-18(3), 343-351, (1982).
- [8] S. Kobayashi, Y. Yamamoto, M. Ito, and T. Kimura, Direct frequency modulation in AlGaAs semiconductor lasers, *IEEE J. Quantum Electron.*, QE-18(4), 582-595, (1982)
- [9] T. Ihegami, Spectrum broadening and tailing effect in directly modulated injection lasers, *First European Conf. on Optical Fiber Commun.*, London, 111-112, (1975).
- [10] K. Nagano, M. Maeda and K. Saito, Sinusoidal modulation characteristics of bur-

- ied heterostructure lasers. Trans. IECE Japan, E61(6), 441-445, (1978).
- [11] H. Nishi, H. Kuwahara and K. Hanamitsu, A semiconductor laser with flat frequency response up to 2 Ghz. Trans. IECE Japan, E61(3), 128-132, (1978).
 - [12] S. Kobayashi, Y. Yamamoto, M. Ito and T. Kimuru, Direct frequency modulation in AlGaAs semiconductor lasers. IEEE J. Quantum Electron., QE-18(4), 582-595, (1982).
 - [13] T. Kimura and Y. Yamamoto, Review: progress of coherent optical fiber communication systems. Opt. and Quantum Electron., 15, 1-39, (1983).
 - [14] H. Tanaka, M. Suzuki and Y. Matsushima, IEEE J. Quantum Electron., QE-29, 1708, (1993).
 - [15] Y. Abe, K. Kishino, Y. Suematsu and S. Arai, GaInAsP/InP integrated laser with butt-jointed built-in distributed-Bragg-reflection waveguide, Electron. Lett., 17(25), 945-947, (1981).
 - [16] Y. Tohmori, X. Jiang, and S. Arai, Novel structure GaInAsP/InP 1.5-1.6 μm bundle integrated-guide (BIG) distributed Bragg reflector laser, Jpn. J. Appl. Phys., 24(6), L399-L401, (1985).
 - [17] Y. Suemastu, M. Yamada and K. Hayashi, A multi-heterostructure AlGaAs laser with integrated twin guide, Proc. IEEE(Lett.), 63(1), (1975).
 - [18] Y. Suemastu, M. Yamada and K. Hayashi, Integrated twin-guide AlGaAs laser with multi-heterostructure, IEEE J. Quantum Electron., QE-11(7), 457-460, (1975).
 - [19] K. Kishino, Y. Suematsu, k.Utaka and H. Kawanishi, Monolithich integration of laser and amplifier/detector by twin-guide structure. Japan. J. Appl. Phys., 17(3), 589-590, (1978).
 - [20] T. Tanbun-ek, S. Arai, F. Koyama, Lowthreshold current CW operation of GaInAsP/InP buried heterostructure distribtd Bragg-reflector integrated-twin-guide laser emitting at 1.6 μm . Electron. Lett. 17(25), 967-968, (1981).
 - [21] S. Sinha, R. V. Ramaswamy, X. Cao and U. Das, Tapered waveguide interconnect by zinc diffusion induced layer disordering of quantum wells, LEOS Summer Topical Meeting on Integrated Optoelectronics, Paper THC3, Santa Barbara, (1992).

- [22] H. S. Kim, S. Sinha, and R. V. Ramaswamy, An MQW-SQW tapered waveguide transition, *IEEE Photonics Technol. Lett.*, 5, 1049-1052, (1993)
- [23] S. K. Han, S. Sinha and R. V. Ramaswamy, Integration of a tapered waveguide with an electroabsorption multi-quantum well modulator, *Proc. on Integrated Photonics Research (IPR'94)*, San Francisco, CA, Feb., 160-162, (1994).
- [24] H. C. Casey Jr. and M. B. Panish, *Heterostructure Lasers*, Academic, New York, (1978).
- [25] W. X. Zou, Z. M. Chuang, K-K. Law, N. Dagli, L. A. Coldren and J. L. Merz, Analysis and optimization of graded-index separate-confinement heterostructure waveguide for quantum well lasers, *J. Appl. Phys.*, 69(5), 2857-2861, (1991).
- [26] D. C. Liu, C. P. Lee, C. M. Tsai, T. F. Lei, J. S. Tsang, W. H. Chiang, and Y. K. Tu, Role of cladding layer thicknesses on strained=layer InGaAs/GaAs single and multiple quantum well lasers, *J. Appl. Phys.*, 73(12), 8027-8034, (1993).
- [27] M. Born and E. Wolf, *Principles of Optics*, Pergamon, New York , (1959)
- [28] M. I. Nathan, W. P. Dumke, G. Burns, Stimulated emission of radiation from GaAs p-n junctions, *Appl. Phys. Lett.*, 1(3), 62, (1962).
- [29] M. Quist, R. H. Rediker, R. J. Keyes, Semiconductor maser of GaAs, *Appl. Phys. Lett.*, 1(4), 91, (1962).
- [30] H. Kroemer, A proposed class of hetero-junction injection lasers, *Proc. IEEE*, 51(12), 1782, (1963).
- [31] Zh. I. Alferov, V. M. Andreev, E. L. Portnoi, and M. K. Trukan, AlAs-GaAs hetero-junction injection lasers with a low room-temperature threshold, *Fiz. Tekh. Poluprov.*, 3, 1328, (1969) (*Sov. Phys. Semicond.*, 3, 1107, 1970)
- [32] I. Hayashi, M. B. Panish, P. W. Foy, and A. Sumski, Junction lasers which operate continuously at room temperature, *Appl. Phys. Lett.*, 17(3), 109, (1970).
- [33] M. B. Panish, H. C. Casey, Jr., S. Sumski, and P. W. Foy, Reduction of threshold current density in GaAs-Al_xGa_{1-x}As heterostructure lasers by separate optical confinement and carrier confinement, *Appl. Phys. Lett.*, 22, 590, (1971)
- [34] M. Nakamura, A. Aiki, J. Umeda, and A. Yariv, CW operation of distributed-feed-

- back GaAs-GaAlAs diode lasers at temperatures up to 300 K, *Appl. Phys. Lett.*, 27, 403-405, (1975).
- [35] S. W. Corzine, R.-H. Yan, L. A. Coldren, Optical gain in III-V bulk and quantum well semiconductors. In *Quantum Well Lasers*, P. S. Zory ed., Academic Press, New York, (1993).
 - [36] R. D. Dupuis, P. D. Dapkus, N. Holonyak, Jr., E. A. Rezek, and R. Chin, Room temperature operation of quantum well $\text{Ga}_{1-x}\text{Al}_x\text{As}$ laser diodes grown by metalorganic chemical vapor deposition, *Appl. Phys. Lett.* 32, 295-297, (1978)
 - [37] W. T. Tsang, C. Weisbuch, R. C. Miller, and R. Dingle, Current injection GaAs- $\text{Al}_x\text{Ga}_{1-x}\text{As}$ multi-quantum-well heterostructure lasers prepared by molecular beam epitaxy, *Appl. Phys. Lett.* 35, 673-675. (1979).
 - [38] W. T. Tsang, Extremely low threshold (AlGa)As modified multiquantum well heterostructure lasers grown by molecular-beam epitaxy, *Appl. Phys. Lett.*, 39, 786-788, (1981).
 - [39] W. T. Tsang, Extremely low threshold (AlGa)As graded-index waveguide separate-confinement heterostructure lasers grown by molecular-beam epitaxy, *Appl. Phys. Lett.*, 40, 217-219, (1982).
 - [40] D. Marcuse, Radiation losses of dielectric slab waveguides, *Bell Sys. Tech. J.*, 49, 273-290, (1970).
 - [41] A. F. Milton and W. K. Burns, Tapered velocity couplers for integrated optics design, *Appl. Optics*, 14, 1207-1212, (1975)
 - [42] H. S. Kim, S. Sinha, and R. V. Ramaswamy, An MQW-SQW tapered waveguide transition, *IEEE Photonics Technol. Lett.*, vol. 5, 1049-1052, (1993)
 - [43] S. K. Han, M. Subramanian, S. Sinha and R. V. Ramaswamy, Fluorine implantation induced tapered waveguide interconnect, *Appl. Phys. Lett.*, vol. 63, 2735-2737, (1993).
 - [44] F. C. Frank and D. Turnbull, Mechanism of diffusion of copper in germanium, *Phys. Rev.*, 104(3), 617-618, (1956)
 - [45] R. L. Longini, Rapid zinc diffusion in GaAs, *Solid State Electron.*, 5, 127-130,

(1962).

- [46] B. Tuck and M. A. Kadhim, Anomalous diffusion profiles of Zinc in GaAs, *J. Material. Sci.*, 7, 581-591, (1972).
- [47] A. H. van Ommen, Examination of models for Zn diffusion in GaAs, *J. Appl. Phys.*, 54, 5055-5058, (1983).
- [48] M. N. O. Sadiku, *Numerical Techniques in Electromagnetics*, CRC Press, Boca Raton, FL, 139, (1992).
- [49] S. K. Ageno and R. J. Roedel, Diffusion of Zn into $\text{Ga}_{1-x}\text{Al}_x\text{As}$, *Appl. Phys. Lett.*, 47(11), 1193-1195, (1985).
- [50] N. Nordell, P. Ojala, W. H. van Berlo, G. Landgren and M. K. Linnarsson, Diffusion of Zn and Mg in AlGaAs/GaAs structures grown by metalorganic vapor-phase epitaxy, *J. Appl. Phys.*, 67, 778-786, (1990).
- [51] W. D. Laidig, N. Holonyak, Jr., M. D. Camras, K. Hess, J. J. Coleman, P. D. Dapkus, and J. Bardeen, *Appl. Phys. Lett.*, 38, 776, (1981).
- [52] W. D. Laidig, N. Holonyak, Jr., J. J. Coleman and P. D. Dapkus, Induced disorder of AlAs-AlGaAs-GaAs quantum-well heterostructures, *J. Electron. Materials*, 11, 1-20, (1982).
- [53] J. A. van Vechten, Intermixing of an AlAs-GaAs superlattice by Zn diffusion, *J. Appl. Phys.*, 53, 7082-7084, (1982).
- [54] H. Iguchi, Atomic diffusion mediated by intrinsic point defects in GaAs and $\text{Al}_x\text{Ga}_{1-x}\text{As}$ -GaAs superlattices, *J. Mater. Res.*, 6, 1542-1552, (1991)
- [55] S. R. Tatti, S. Mitra, and J. P. Stark, A proposed model to explain impurity-induced layer disordering in AlAs-GaAs heterostructures, *J. Appl. Phys.*, 65, 2547-2549, (1989).
- [56] D. G. Deppe and N. Holonyak, Atom diffusion and impurity-induced layer disordering in quantum well III-V semiconductor heterostructures, *J. Appl. Phys.*, 64, R93-R113, (1988).
- [57] T. Y. Tan and U. Goesele, Diffusion mechanisms and superlattice disordering in

- GaAs, Mater. Sci. Eng. B1, 47-65, (1988).
- [58] Harrison and H. P. Ho, Zn diffusion-induced disorder in AlAs/GaAs superlattices, Semicond. Sci. Technol., 4, 841-846, (1989)
 - [59] N. H. Ky, J. D. Ganiere, and M. Gaihanou, B. Blanchard, L. Pavesi, G. Burri, D. Araujo and F. K. Reinhart, Self-interstitial mechanism for Zn diffusion-induced disordering of GaAs/Al_xGa_{1-x}As (x=0.1-1) multiple-quantum-well structures, J. Appl. Phys., 73(8), 3769-3781, (1993).
 - [60] B. Tuck, Atomic Diffusion in III-V Semiconductor, Adam Hilger, 28, (1988).
 - [61] J. W. Lee and W. D. Laidig, Diffusion and interdiffusion in Zn disordered AlAs-GaAs superlattice, J. Electronic. Material., vol.3, 147-165, (1984)
 - [62] I. Harrison, Zn diffusion effects in GaAs/AlAs, in Properties of Gallium Arsenide, EMIS Group ed., 357, (1990).
 - [63] M. D. Camras, N. Holonyak, Jr., R. D. Burnham, W. Streifer, D. R. Scifres, T. L. Paoli, and C. Lindstrom, Wavelength modification of Al_xGa_{1-x}As quantum well heterostructure lasers by layer diffusion, J. Appl. Phys., 54(10), 5637-5641, (1983).
 - [64] J. Cibert, P. M. petroff, D. J. Werder, S. J. Pearton, A. C. Gossard, and J. H. English, Kinetics of implantation enhanced interdiffusion of Ga and Al at GaAs-Ga_xAl_{1-x}As interfaces, Appl. Phys. Lett., 49(4), 223-225, (1986).
 - [65] J. Crank, The Mathematics of Diffusion, 2nd ed. Clarendon, Oxford, 144, (1975).
 - [66] E. P. Zucker, A. Hashimoto, and N. Watanabe, Ion-implanted Zn diffusion and impurity-induced disordering of an AlGaAs superlattice, Appl. Phys. Lett., 54(6), 564-566, (1989).
 - [67] J. Ihm, P. K. Lam, and M. L. Cohen, Electronic structure of the [001] InAs-GaSb superlattices, Phys. Rev. B 20, 4120-4125, (1979).
 - [68] J. N. Shulman and Y. C. Chang, Bandmixing in semiconductor superlattices, Phys. Rev. B 31, 2056-2068, (1985).
 - [69] K. B. Kahen and J. P. Lebrton, Optical constants of GaAs-Al_xGa_{1-x}As superlattices and multiple quantum wells, Phys. Rev. B, 33, 5465-5472, (1986).

- [70] R. E. Smith, L. A. Moltor and M. Dutta, Evaluation of refractive index approxiations used for mode determination in multiple quantum well slab waveguides, IEEE J. Quantum Electron., 27, 1119-1122, (1991).
- [71] M. A. Fromowitz, Refractive index of $\text{Ga}_{1-x}\text{Al}_x\text{As}$, Solid State Communi., 15, 59-63, (1974).
- [72] R. L. Liboff, Introductory Quantum Mechanics, Holden-Day, Oakland, (1980).
- [73] A. K. Ghatak and K. Thyagarajan, Optical Electronics, Cambridge University Press, New York, (1989).

BIOGRAPHICAL SKETCH

Suning Xie was born in Jiangsu, China, in November 1961. He received the B.E. and M.E. degrees in electronic engineering from Tsinghua University, Beijing, China, in 1984 and 1987, respectively.

From 1987 to 1989, he was employed as a researcher by China Academy of Electronics and Information Technology, Beijing. From 1990 to 1992, he was a visiting researcher with Heinrich Hertz Institute of Communications Technology, Berlin, Germany. Since 1993, he has been with the Photonics Research Laboratory, Department of Electrical and Computer Engineering, University of Florida, Gainesville, Florida, where he is a Ph.D. candidate and a graduate research assistant. His research interests include active and passive guided-wave optoelectronic devices and their integration in III-V semiconductors.

I certify that I have read this study and that in my opinion it conforms to acceptable standards of scholarly presentation and is fully adequate, in scope and quality, as a dissertation for the degree of Doctor of Philosophy.



Ramu V. Ramaswamy, Chairman
Professor of Electrical and Computer Engineering

I certify that I have read this study and that in my opinion it conforms to acceptable standards of scholarly presentation and is fully adequate, in scope and quality, as a dissertation for the degree of Doctor of Philosophy.



Sheng S. Li
Professor of Electrical and Computer Engineering

I certify that I have read this study and that in my opinion it conforms to acceptable standards of scholarly presentation and is fully adequate, in scope and quality, as a dissertation for the degree of Doctor of Philosophy.



Arnost Neugroschel
Professor of Electrical and Computer Engineering

I certify that I have read this study and that in my opinion it conforms to acceptable standards of scholarly presentation and is fully adequate, in scope and quality, as a dissertation for the degree of Doctor of Philosophy.



Ewen Thomson
Associate Professor of Electrical and Computer Engineering

I certify that I have read this study and that in my opinion it conforms to acceptable standards of scholarly presentation and is fully adequate, in scope and quality, as a dissertation for the degree of Doctor of Philosophy.



David Tanner
Professor of Physics

This dissertation was submitted to the Graduate Faculty of the College of Engineering and to the Graduate School and was accepted as partial fulfillment of the requirements for the degree of Doctor of Philosophy.

December 1996



Winfred M. Phillips
Dean, College of Engineering

Karen A. Holbrook
Dean, Graduate School

- [70] R. E. Smith, L. A. Moltor and M. Dutta, Evaluation of refractive index approxiations used for mode determination in multiple quantum well slab waveguides, IEEE J. Quantum Electron., 27, 1119-1122, (1991).
- [71] M. A. Fromowitz, Refractive index of $\text{Ga}_{1-x}\text{Al}_x\text{As}$, Solid State Communi., 15, 59-63, (1974).
- [72] R. L. Liboff, Introductory Quantum Mechanics, Holden-Day, Oakland, (1980).
- [73] A. K. Ghatak and K. Thyagarajan, Optical Electronics, Cambridge University Press, New York, (1989).

BIOGRAPHICAL SKETCH

Suning Xie was born in Jiangsu, China, in November 1961. He received the B.E. and M.E. degrees in electronic engineering from Tsinghua University, Beijing, China, in 1984 and 1987, respectively.

From 1987 to 1989, he was employed as a researcher by China Academy of Electronics and Information Technology, Beijing. From 1990 to 1992, he was a visiting researcher with Heinrich Hertz Institute of Communications Technology, Berlin, Germany. Since 1993, he has been with the Photonics Research Laboratory, Department of Electrical and Computer Engineering, University of Florida, Gainesville, Florida, where he is a Ph.D. candidate and a graduate research assistant. His research interests include active and passive guided-wave optoelectronic devices and their integration in III-V semiconductors.

I certify that I have read this study and that in my opinion it conforms to acceptable standards of scholarly presentation and is fully adequate, in scope and quality, as a dissertation for the degree of Doctor of Philosophy.



Ramu V. Ramaswamy, Chairman
Professor of Electrical and Computer Engineering

I certify that I have read this study and that in my opinion it conforms to acceptable standards of scholarly presentation and is fully adequate, in scope and quality, as a dissertation for the degree of Doctor of Philosophy.



Sheng S. Li
Professor of Electrical and Computer Engineering

I certify that I have read this study and that in my opinion it conforms to acceptable standards of scholarly presentation and is fully adequate, in scope and quality, as a dissertation for the degree of Doctor of Philosophy.



Arnost Neugroschel
Professor of Electrical and Computer Engineering

I certify that I have read this study and that in my opinion it conforms to acceptable standards of scholarly presentation and is fully adequate, in scope and quality, as a dissertation for the degree of Doctor of Philosophy.



Ewen Thomson
Associate Professor of Electrical and Computer Engineering

I certify that I have read this study and that in my opinion it conforms to acceptable standards of scholarly presentation and is fully adequate, in scope and quality, as a dissertation for the degree of Doctor of Philosophy.



David Tanner
Professor of Physics

This dissertation was submitted to the Graduate Faculty of the College of Engineering and to the Graduate School and was accepted as partial fulfillment of the requirements for the degree of Doctor of Philosophy.

December 1996



Winfred M. Phillips
Dean, College of Engineering

Karen A. Holbrook
Dean, Graduate School